The Journal of Chemical Physics

AIP Publishing

Spectrally tunable infrared plasmonic $F,Sn:In_2O_3$ nanocrystal cubes EP

Cite as: J. Chem. Phys. **152**, 014709 (2020); https://doi.org/10.1063/1.5139050
Submitted: 17 November 2019 . Accepted: 13 December 2019 . Published Online: 07 January 2020

Shin Hum Cho, Kevin M. Roccapriore, Chandriker Kavir Dass, Sandeep Ghosh, Junho Choi, Jungchul Noh, Lauren C. Reimnitz, Sungyeon Heo, Kihoon Kim, Karen Xie, Brian A. Korgel, Xiaoqin Li, Joshua R. Hendrickson, Jordan A. Hachtel, and Delia J. Milliron

COLLECTIONS

Paper published as part of the special topic on Emerging Directions in Plasmonics and JCP Editors' Choice 2019
Note: This paper is part of the JCP Special Topic on Emerging Directions in Plasmonics.

EP This paper was selected as an Editor's Pick

View Online Export Citation CrossMark

ARTICLES YOU MAY BE INTERESTED IN

Structure and phase behavior of polymer-linked colloidal gels
The Journal of Chemical Physics **151**, 124901 (2019); https://doi.org/10.1063/1.5119359

Properties of quantum dots coupled to plasmons and optical cavities
The Journal of Chemical Physics **151**, 210901 (2019); https://doi.org/10.1063/1.5124392

The Journal of Chemical Physics **PLAS2020**, 014709 (2020); https://doi.org/10.1063/1.5139050@jcp.2020.PLAS2020.issue-1


Lock-in Amplifiers
Find out more today
Zurich Instruments

© 2020 Author(s).

The Journal of Chemical Physics ARTICLE scitation.org/journal/jcp

Spectrally tunable infrared plasmonic F,Sn:In_2O_3 nanocrystal cubes

Cite as: J. Chem. Phys. **152**, 014709 (2020); doi: 10.1063/1.5139050
Submitted: 17 November 2019 • Accepted: 13 December 2019 •
Published Online: 7 January 2020

Shin Hum Cho,[1] Kevin M. Roccapriore,[2] Chandriker Kavir Dass,[3,4] Sandeep Ghosh,[1] Junho Choi,[5] Jungchul Noh,[1] Lauren C. Reimnitz,[1] Sungyeon Heo,[1,6] Kihoon Kim,[1] Karen Xie,[1] Brian A. Korgel,[1] Xiaoqin Li,[5] Joshua R. Hendrickson,[3] Jordan A. Hachtel,[2] and Delia J. Milliron[1,a)]

AFFILIATIONS

[1] McKetta Department of Chemical Engineering, The University of Texas at Austin, Austin, Texas 78712, USA
[2] Center for Nanophase Materials Sciences, Oak Ridge National Laboratory, Oak Ridge, Tennessee 37831, USA
[3] Sensors Directorate, Air Force Research Laboratory, Wright-Patterson AFB, Dayton, Ohio 45433, USA
[4] KBRwyle, Beavercreek, Ohio 45431, USA
[5] Department of Physics, Center for Complex Quantum Systems, The University of Texas, Austin, Texas 78712, USA
[6] Department of Electrical Engineering, Princeton University, Princeton, New Jersey 08544, USA

Note: This paper is part of the JCP Special Topic on Emerging Directions in Plasmonics.

[a)] **Author to whom correspondence should be addressed:** milliron@che.utexas.edu

ABSTRACT

A synthetic challenge in faceted metal oxide nanocrystals (NCs) is realizing tunable localized surface plasmon resonance (LSPR) near-field response in the infrared (IR). Cube-shaped nanoparticles of noble metals exhibit LSPR spectral tunability limited to visible spectral range. Here, we describe the colloidal synthesis of fluorine, tin codoped indium oxide (F,Sn:In_2O_3) NC cubes with tunable IR range LSPR for around 10 nm particle sizes. Free carrier concentration is tuned through controlled Sn dopant incorporation, where Sn is an aliovalent *n*-type dopant in the In_2O_3 lattice. F shapes the NC morphology into cubes by functioning as a surfactant on the {100} crystallographic facets. Cube shaped F,Sn:In_2O_3 NCs exhibit narrow, shape-dependent multimodal LSPR due to corner, edge, and face centered modes. Monolayer NC arrays are fabricated through a liquid-air interface assembly, further demonstrating tunable LSPR response as NC film nanocavities that can heighten near-field enhancement (NFE). The tunable F,Sn:In_2O_3 NC near-field is coupled with PbS quantum dots, via the Purcell effect. The detuning frequency between the nanocavity and exciton is varied, resulting in IR near-field dependent enhanced exciton lifetime decay. LSPR near-field tunability is directly visualized through IR range scanning transmission electron microscopy-electron energy loss spectroscopy (STEM-EELS). STEM-EELS mapping of the spatially confined near-field in the F,Sn:In_2O_3 NC array interparticle gap demonstrates elevated NFE tunability in the arrays.

Published under license by AIP Publishing. https://doi.org/10.1063/1.5139050

INTRODUCTION

Colloidal synthesis of doped metal oxide nanocrystals (NCs) has emerged recently as a route for expanding localized surface plasmon resonance (LSPR) to the infrared (IR) range.[1] With a suitable metal oxide NC host material, free electron compensating point defects are engineered by introducing *n*-type dopants. Doping strategies in plasmonic metal oxide NCs involve aliovalent cation substitution (e.g., Sn:In_2O_3,[2] Al:ZnO,[3] and In:CdO[4] NCs) and anionic fluorine doping (e.g., F,In:CdO,[5] F,Sn:In_2O_3,[6] and F:In_2O_3 NCs[7]) in metal oxide NC host lattices. Spectral advantages are nascent in doped metal oxide NC systems. Metal nanoparticles intrinsically possess high free-carrier concentrations exceeding 10^{23} cm^{-3}, leading to LSPR optical response restricted to the visible region of the electromagnetic spectrum.[8,9] Spectral tunability relies on increasing particle size in such metal classes of NCs to red-shift LSPR modes,[10,11] adding dimensional constraints to nanoassembly architectures. Alternatively, doped metal oxide NCs relieve particle size constraints, expanding tunable IR range LSPR through variable dopant incorporation with free-carrier concentration control in the 10^{21} cm^{-3} range.[12,13] Intraband and interband transition effects optically observed in Au nanoparticles[14] can be circumvented in doped metal oxide NCs. Due to low free-carrier concentrations, the LSPR located in the IR range is well separated from the UV-range optical band edge in wide-bandgap metal oxide materials.[1,15]

Shape-dependent optical properties need to be further developed in doped metal oxide classes of NCs to achieve complete spectral control in the IR. Colloidal Au and Ag cube nanoparticles sculpted by faceting agents led to the observation of shape-dependent LSPR and enhanced electromagnetic near-fields at morphological discontinuities.[16,17] Halogen anions are capping agents that have been used for shape control of metal[18] and metal chalcogenide[19,20] classes of NCs, while shape control in LSPR active metal oxide[21] NCs is only recently being realized.[22] Morphologies reported for colloidal Au and Ag nanoparticles include cubes,[16,23,24] where faceted nanoparticles provide shape-dependent LSPR properties not observed in spherical particles. This includes strong near-field enhancement (NFE) hot spots around corners and edges[17,25] that, in well-established metal nanoparticles, have been leveraged for plasmonic nanoantennas[26] and surface-enhanced Raman spectroscopy (SERS).[27,28,18] Despite well-defined studies in noble metal NCs, limitations in IR range tunability for noble metal NCs are inherent. This includes a fixed high free carrier concentration, intraband or interband losses contributing to spectral linewidth, and spectral tunability that depends on particle size. Combining spectral tunability with high NFE may be approached through alternative materials for optimal performance in the IR spectral range.

We advance LSPR spectral tunability in the IR range while preserving highly faceted cube morphology via codoped F,Sn:In_2O_3 NCs. In our previous work, shape control in this developing class of nanocrystalline materials was investigated using fluorine as an *n*-type dopant and as a faceting agent in fluorine-doped indium oxide (F:In_2O_3) cube NCs, yet broad LSPR tuning was not realized.[7] Leveraging recent synthetic developments employing a continuous slow injection of indium and dopant precursors into a heated reaction solution, a high degree of NC shape and size control can be realized.[29,30] The resulting LSPR properties with Sn and F codopants along with faceting effects are investigated here. We show that the cationic Sn dopant is simultaneously incorporated with anionic F into F surface-passivated, cube-shaped In_2O_3 NCs to spectrally tune LSPR. The anionic F dopant suppresses divalent scattering centers, leading to enhanced quality factors and narrow LSPR spectral linewidths. Controlled Sn dopant introduction in NCs allows tunable carrier concentrations around 10^{21} cm^{-3}, resulting in synthetic access to IR range LSPR tunability control with high quality factors in NC solvent dispersions.

Having attained advantages in IR range LSPR tunability, F,Sn:In_2O_3 NCs are further self-assembled to fabricate dense plasmonic NC array films. Relieving spatial restrictions from size dependent LSPR tuning that impacted prior studies of noble metal nanoparticles, LSPR tunable F,Sn:In_2O_3 NCs allow realization of densely packed nanogap cavities in monolayer film assemblies while retaining small particle size. Spectrally tuned dense nanocavity arrays demonstrating NFE can be used to influence the optical properties of other classes of NCs. Based on strides in synthetic chemistry, access to two classes of photophysical light-matter interactions has been achieved over the past decade through colloidal NC synthesis.[31] Excitonic light emission of quantum dot (QD) NCs is possible through quantum confinement effects, allowing photoluminescence (PL) in inorganic semiconductor materials (e.g., CdSe,[32] InP,[33] PbS,[34] and HgS[35]) through exciton electron-hole pair recombination. Meanwhile, confinement of electromagnetic field beyond the diffraction limit has been enabled through free-electron carrier confining in nanoparticles smaller than one fifth of the incident wavelength dimension, allowing LSPR-induced NFE to occur.[36] Such maturation in two classes of NCs allows hierarchical assembly of matter to be achieved. Here, architectures containing PbS QDs and F,Sn:In_2O_3 NCs were fabricated by stacking monolayer films together through a modified liquid-air interface self-assembly method.[37,38] Local and long-range NC ordering was, respectively, observed through scanning electron microscopy (SEM) and small angle X-ray scattering (SAXS), ensuring film uniformity. Self-assembled LSPR tunable F,Sn:In_2O_3 NCs allow a degree of control in nanocavity film NFE by detuning the frequency to enhance PbS QD lifetime decay rates at a photoluminescence (PL) wavelength located in the conventional-band (C-band) low-loss optical telecommunication window.[39,40] Excitonic and plasmonic light-matter interactions can be optically coupled when the materials are spatially in the vicinity of each other via the Purcell effect. Strong NFE from LSPR antennas enhances the PL lifetime decay rate in excitonic materials in the Purcell weak-coupling regime.[26,41] The IR range LSPR near-field of F,Sn:In_2O_3 NC film arrays is observed to influence the exciton decay rate in excitonic PbS QDs through time resolved PL measurements.

The IR range LSPR near-field, expected to be spatially localized around F,Sn:In_2O_3 NCs, is directly visualized through monochromated scanning transmission electron microscopy-electron energy loss spectroscopy (STEM-EELS).[42] With recent improvement in monochromator energy resolution,[43–45] STEM-EELS allows access to plasmonic near-field mapping at increasingly low-energy scales and at nanoscale spatial resolution. The intense IR near-field spatially confined between F,Sn:In_2O_3 NCs in interparticle gaps was directly visualized through EELS mapping. We observe that the F,Sn:In_2O_3 NC ordered array has emergent collective near-field ensemble behavior, unique from localized in-gap confined near-field modes. The collective NC film array ensemble was observed to have a long range spatially delocalized near-field decay length extending from the edges of the NC array. This was further supported by a delocalized mode volume extracted from the analysis of the Purcell enhanced PL decay lifetime in PbS QDs coupled to a F,Sn:In_2O_3 NC film. The synthesized materials and observed optical characteristics led to IR light near-field localization, making F,Sn:In_2O_3 NCs a gateway material in emergent IR near-field enhancement applications.

EXPERIMENTAL METHODS

Materials

Indium(III) acetate [In(ac)$_3$, 99.99%], tin(IV) acetate [Sn(ac)$_4$], lead(II) chloride ($PbCl_2$, 99.999%), sulfur (S, 99.99%), oleic acid (OA, 90%, technical grade), oleyl alcohol (OlAl, 85%, technical grade), octane (98%, reagent grade), 1-butanol (99.9%), ethylene glycol (99.8%), and tetrachloroethylene (99%, anhydrous) were purchased from Sigma-Aldrich. Tin(IV) fluoride (SnF_4, 99%) was purchased from Alfa Aesar, and oleylamine (OlAm, 80%–90%) was purchased from Acros Organics. Hexane (99.9%), acetone (99.5%, Certified ACS), isopropyl alcohol (99.5%, Certified ACS), and methanol (99.8%, Certified ACS) were purchased from Fisher Chemical. Hellmanex-III cleaning solution was purchased from Hellma Analytics. All chemicals were used as received without any further purification.

Fluorine doped indium tin oxide ($F,Sn:In_2O_3$) cube synthesis

All synthesis procedures are undertaken by employing standard Schlenk line techniques using a modification of previously reported methods for a continuous slow injection synthesis of indium oxide NCs.[29,46] In(acac)$_3$ 1342.97 mg (4.6 mmol), SnF_4 48.68 mg (5%, 0.25 mmol), Sn(ac)$_4$ 53.23 mg (3%, 0.15 mol), and oleic acid (10 ml) are loaded in a three-neck round-bottom flask in a N_2-filled glovebox. The precursors are stirred with a magnetic bar at 600 rpm and degassed under vacuum at 120 °C for 15 min. The injection solution is added at a rate of 0.2 ml/min into 13 ml of oleyl alcohol maintained at 290 °C vented with a 19-gauge needle under inert N_2 gas flow. The reaction mixture turns blue a few minutes into the injection. Subsequently, growth is terminated by removal of the heating mantle and cooled by blowing air on the three-neck flask vessel. The NCs are dispersed in hexane, then ethanol antisolvent is added, and the mixture is centrifuged at 7500 rpm for 10 min. The washing procedure is repeated 3 times, and the NCs are redispersed in 10 ml of hexane. The resultant NC dispersion is centrifuged at 2000 rpm for 3 min to remove nondispersible aggregates, and the supernatant is collected as the NC stock sample. Larger sized NCs were synthesized by controlling the volume of injection solution (1–20 ml) while keeping other reaction parameters identical. A concentration series [0%–15% Sn(ac)$_4$] of doped $F,Sn:In_2O_3$ NCs was synthesized by controlling the Sn(ac)$_4$ to In(ac)$_3$ molar precursor ratio, while SnF_4 was maintained at 5% molar ratio, keeping other reaction parameters identical. The Sn doping concentration in the NCs is characterized by inductively coupled plasma-atomic emission spectroscopy (ICP-AES) on a Varian 720-ES ICP optical emission spectrometer after digesting the NCs with aquaregia solution (a mixture of 35% concentrated HCl and 70% HNO_3 in a 3:1 ratio, respectively).

Lead sulfide (PbS) QD synthesis

The synthetic procedures reported by Weidman *et al.* employing standard Schlenk line techniques are used to synthesize PbS QDs.[34] A sulfur hot injection solution is prepared in a N_2 glovebox with sulfur 20 mg in oleylamine 3.75 ml stirred at 120 °C for 30 min. A lead solution is prepared by combining $PbCl_2$ 2.50 g (9 mmol) with oleylamine 7 ml in a three-neck flask. The solution is degassed at 120 °C for 30 min and pressurized with N_2 until the temperature is stable. 2.25 ml (0.375 mmol) of prepared sulfur solution is swiftly injected into the lead solution, and the reaction is allowed to proceed for 5 min. A washing procedure is repeated 3 times by dispersion in 20 ml of hexane, precipitation with alcohol antisolvents (10 ml butanol and 5 ml methanol), and centrifugation at 4000 rpm for 5 min. Oleic acid 2 ml is added in between wash steps to promote colloidal stability. Excess $PbCl_2$ precipitates are centrifuged out at 4000 rpm for 3 min, and the PbS QD supernatant in hexane is kept as a stock solution.

Film fabrication

Diced (1 × 1 cm^2) undoped silicon (Si) substrates are sonicated in solvents for 30 min in the following order: Hellmanex-III (5% by volume) in deionized (DI) water (followed by a DI water rinse prior to the next step), acetone, isopropyl alcohol, and hexane. Diluted PbS QD solution (5 mg/ml) in hexane:octane 1:1 by solvent volume is spincoated onto a Si substrate at 1500 rpm for 90 s, then at 4000 rpm for 2 min to promote drying, producing monolayer PbS films. $F,Sn:In_2O_3$ NC monolayers over PbS films are fabricated by modification of the liquid-air interface assembly described earlier by Dong *et al.*[37,38] A Teflon well (2 × 4 × 4 cm^3) was custom made with a ball valve at the trough bottom to minimize liquid-air interface perturbation during transfer of the NC assembly to the substrate upon liquid drainage. A Si substrate with a PbS QD film is placed on an elevated (1 cm) Teflon platform immersed in an ethylene glycol subphase. 100 μl of dilute $F,Sn:In_2O_3$ NC dispersion in hexane (1 mg/ml) is dropcast onto the subphase surface with a pipette and the trough is covered with a glass slide. $F,Sn:In_2O_3$ NC monolayer self-assembly is allowed to proceed while hexane gradually evaporates for a duration of 15 min. The ethylene glycol subphase is allowed to drain out of the trough by opening the ball valve with minimal perturbation to the self-assembled NC film. Residual ethylene glycol on the film is dried in a room temperature vacuum oven for 24 h. The same procedure is used for NC array fabrication over SiN TEM supports but in the absence of PbS QDs. Surface organic ligands are removed by plasma cleaning under Ar for at least 15 min for TEM support samples.

UV-Vis-NIR/FTIR spectra measurement

UV-Vis-NIR spectral measurement is conducted using an Agilent Cary 5000 UV-Vis-NIR spectrophotometer, and FTIR spectral measurement is conducted using a Bruker Vertex 70 FTIR at 4 cm^{-1} scan resolution for both solution and film samples. Hexane dispersed NCs are vacuum dried, redispersed in tetrachloroethylene (TCE), and loaded into a 0.05 cm pathlength liquid cell with KBr windows for solvent dispersion UV-Vis-NIR and FTIR measurements.

X-ray diffraction analysis

X-ray diffraction (XRD) samples are prepared by drop-casting 20 mg/ml solution of $F,Sn:In_2O_3$ NCs on Si substrates. The data are collected with a Rigaku MiniFlex 600 X-ray diffractometer using Cu Kα radiation (1.54 Å). High resolution of the (222) diffraction peak is measured in a Rigaku R-Axis Spider diffractometer using Cu Kα radiation at 1.54 Å, with NC powders mounted in a mineral oil loaded Kapton loop. Rietveld refinement is conducted using the GSAS-II software.[47]

Published under license by AIP Publishing

Electron microscopy

F,Sn:In_2O_3 NCs are characterized by a Hitachi S5500 scanning electron microscope (SEM). Particle size analysis is done with ImageJ with a 100 particle count. High resolution transmission electron microscopy (HRTEM) images and selected area electron diffraction (SAED) are acquired with a JEOL 2010F TEM at 200 kV. Elemental spectrum acquisition of F,Sn:In_2O_3 cubes dropcast on silicon substrates is carried out using a Hitachi S5500 SEM with a Bruker XFlash EDX detector attachment at 5 kV. Elemental deconvolution was performed with Bruker Quantax software reference at zero-tilt angle P/B-ZAF correction.

X-ray photoelectron spectroscopy (XPS)

Samples are prepared by drop casting NC dispersions on silicon substrates and the measurements are performed in a Kratos Axis Ultra DLD spectrometer with a monochromatic Al Kα source (1486.6 eV). Wide survey scans are acquired at an analyzer pass energy of 80 eV, and the high-resolution narrow region scans are performed at a pass energy of 20 eV with steps of 0.1 eV. Spectral acquisitions are performed with a photoelectron take-off angle of 0° with respect to the surface normal and pressure in the analysis chamber maintained at around 10^{-9} torr. Data analysis is performed in the CasaXPS software using the Kratos relative sensitivity factor library. The binding energy (BE) scale is internally referenced to the C 1s peak (BE for C-C = 284.8 eV).

Grazing Incidence Small-Angle X-ray Scattering (GISAXS)

Grazing incidence small-angle X-ray scattering (GISAXS) is performed using a SAXSLAB Ganesha SAXS system. Assembled NC film samples on Si substrates are loaded in the SAXS system vacuum chamber. Monochromatic X-ray radiation of wavelength of 1.54 Å is used. The incident angle of the beam was 0.2°. Small-angle scattered photons are collected with a PILATUS3 R 300 K detector with 487 × 619 pixels and a pixel size of 172 μm × 172 μm positioned at appropriate distances from the sample (1084 mm for GISAXS).

Time-resolved photoluminescence

The samples are pumped with a Coherent Chameleon Ultra Ti:sapphire laser operating at 850 nm and 5 MHz repetition rate, down-converted from 80 MHz using an AOM-based pulse-picker. Excitation and collection are in a reflection geometry using a Mitutoyo NIR 0.42 NA long working distance objective. The collected emission is then sent to a fiber-coupled superconducting nanowire single photon detector (SNSPD) from Single Quantum. Histograms of the SNSPD signal output are made using a PicoQuant HydraHarp 400 ps event timer triggered by the AOM pulse-picker.

Scanning Transmission Electron Microscopy-Electron Energy Loss Spectroscopy (STEM-EELS)

Plasmon near-field mapping is performed in a Nion high energy-resolution monochromated STEM-EELS at the Oak Ridge National Laboratory operated at 60 kV and using a Nion Iris spectrometer.[43,44] Identical energy resolution of 145 cm^{-1} (18 meV) is set to optimize the resolution between the plasmon peaks and the signal in the monochromated beam.

RESULTS AND DISCUSSION

F,Sn:In_2O_3 NC synthesis

The shapes of the F,Sn:In_2O_3 NCs were controlled by varying the molar ratio of SnF_4 to Sn(ac)$_4$ precursors added to the injection solution. This determines the extent of fluorine and tin dopant incorporation into the resulting NC products. F,Sn:In_2O_3 NCs with well-defined morphology were produced for 0%–3% Sn(ac)$_4$ in the growth solution, as illustrated in Fig. 1(a). SEM images show that monodisperse NCs with cubic morphology were obtained exclusively in the presence of SnF_4 at this dopant range. For comparison, synthesis in the absence of SnF_4 and exclusively with Sn(ac)$_4$ dopant precursors was conducted. Spherical Sn:In_2O_3 NCs were observed (Fig. S1), implying that fluorine plays a faceting role in shaping cubic Sn:In_2O_3 NCs. It was observed that higher amounts of SnF_4 led to deterioration of the cubic NC morphology by forming rough facets. In the absence of Sn(ac)$_4$ precursors, the cube morphology is retained at adequate concentrations of SnF_4 (3% and 5%). Yet, NCs with evident rough surfaces attributable to F^- ion induced corrosion pitting[18,22] are observed under excessive SnF_4 addition of 10% molar ratio (Fig. S2). For the sake of retaining high-quality cube shapes in this study, 5% SnF_4 molar precursor ratio is nominally maintained while further addition of Sn(ac)$_4$ as a cationic codoping agent is made to achieve LSPR tunability.

TEM images of F,Sn:In_2O_3 NC cubes from 0% to 3% Sn(ac)$_4$ exhibit well-defined facets, as shown in Fig. 1(a). Fast Fourier transform (FFT) of HRTEM images confirms that F:In_2O_3 NC cubes are single crystalline particles and allows indexing of dominant surface exposed facets [Fig. 1(a), inset]. Observations show that the cubes are terminated with {100} facets of the In_2O_3 cubic bixbyite structure, consistent with previously reported fluorine passivated In_2O_3 NCs.[7] Crystallinity in NCs is well retained over the full Sn(ac)$_4$ dopant range as shown in FFT patterns collected down the $\langle 100 \rangle$ zone axis. Rounded cube morphology appears above a threshold of 4% Sn(ac)$_4$, until NCs become dominantly spherical in shape near 10% Sn(ac)$_4$. The size of the NCs remained consistent with an edge length of 12.6 ± 0.6 nm (Fig. S3), when synthesized with 10 ml of precursor solution injected while the Sn(ac)$_4$ dopant precursor ratio was controllably incremented. Versatility in NC cube size control is demonstrated by varying the amount of precursor solution injected into hot oleyl alcohol solution between 1 and 20 ml. The cubic shape is retained as observed in F,Sn:In_2O_3 NC cube [3% Sn(ac)$_4$] SEM images, and the size trend with variable injection volume is as expected (Fig. S4).

To quantify total F and Sn dopant incorporation into F,Sn:In_2O_3 NCs, inductively coupled plasma-atomic emission spectroscopy (ICP-AES) and energy dispersive X-ray (EDX) spectroscopy were conducted. Since the emitted X-rays have high energy after electron beam penetration, EDX has an effective probe depth of about 200 nm, so the results reflect the overall F composition of the NC ensemble in the drop-casted sample.[7,48] Atomic component quantification [Figs. 1(b) and S5] shows F atomic composition

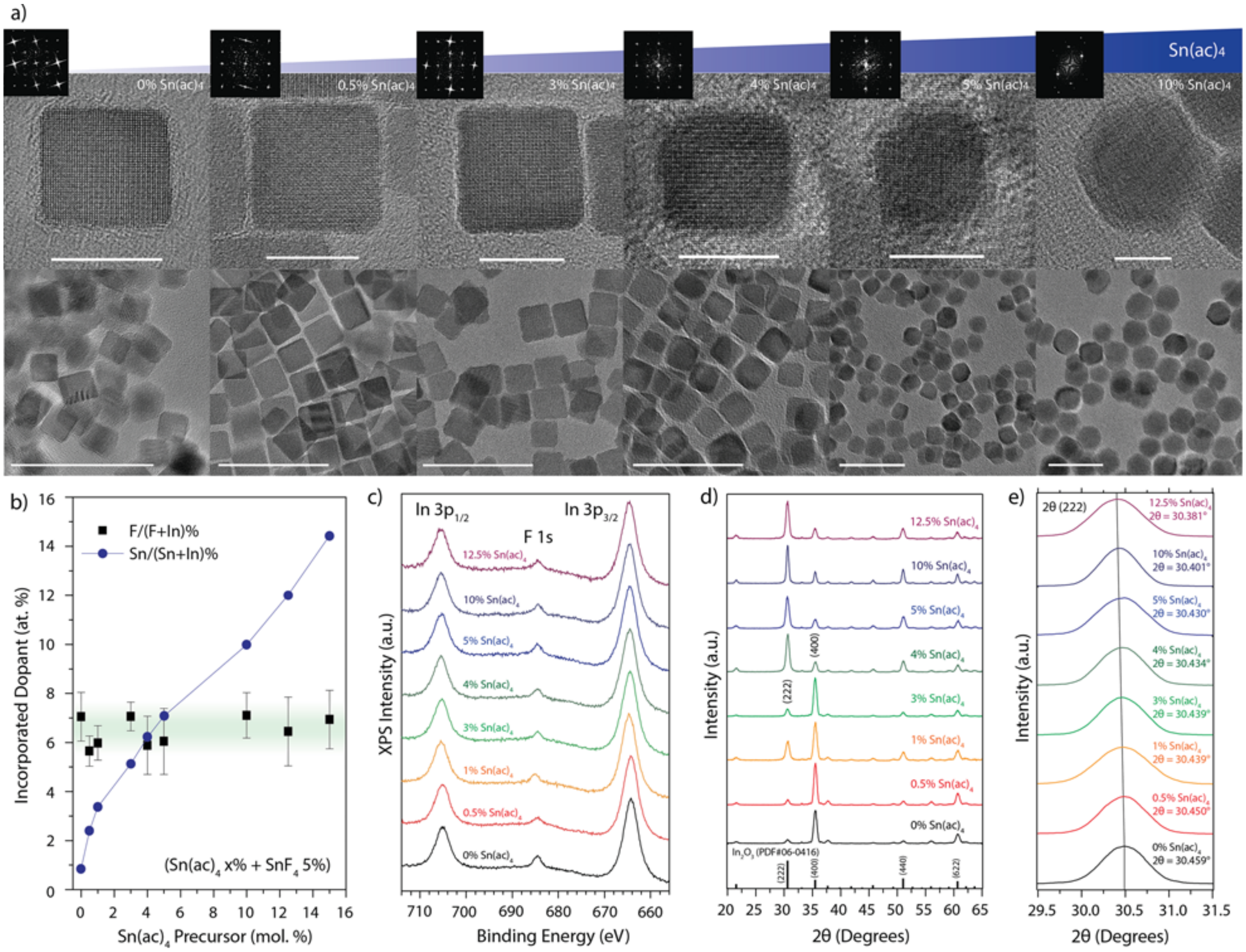

FIG. 1. (a) HRTEM image of F,Sn:In_2O_3 NC with progressively increased 0%–10% Sn(ac)$_4$ and maintained 5% SnF_4 dopant precursor molar ratio. FFT (insets) shows {100} facet orientation of NC cubes, and single particle HRTEM shows NC crystallinity (middle) with scale bars at 10 nm. Wide field view HRTEM image scale bars are at 50 nm (bottom). (b) Dopant incorporation into F,Sn:In_2O_3 NC for F and Sn. The fluorine dopant precursor was maintained at 5% SnF_4, with controlled Sn incorporation at 0%–15% Sn(ac)$_4$ dopant precursor concentration range. (c) XPS spectra of F,Sn:In_2O_3 NC Sn dopant concentration series for F 1s and In 3p. (d) XRD pattern of F,Sn:In_2O_3 NCs, (222) and (400) peaks labeled with In_2O_3 powder reference pattern (PDF No. 00-006-0416). (e) XRD pattern for (222) reflection shows a peak shift indicating lattice expansion as the Sn dopant precursor ratio increases.

being sustained in F,Sn:In_2O_3 NCs around 6.5 at. % as SnF_4 fluorine precursor concentration employed during synthesis is maintained at 5% molar ratio. With Sn peak signatures being in close vicinity to In peaks in EDX, ICP-AES trace metal elemental analysis was employed for Sn dopant quantification. Sn atomic composition in NCs is observed to systematically increase as a function of Sn(ac)$_4$ precursor addition (0%–15%), demonstrating the efficacy of Sn cationic dopant incorporation into the NCs. The Sn dopant incorporation into NCs shows a monotonic increase as Sn(ac)$_4$ is proportionally increased in the precursor injection solution. The substantial increase in Sn dopant incorporation observed between 0% and 1% Sn(ac)$_4$ levels can be attributed to effective liberation of Sn from Sn(ac)$_4$ due to soft binding acetate ligands as compared to harder binding halides when SnF_4 is the only dopant precursor.[1,49,50]

NC surface characterization

Fluoride anions (F^-) have been described as facet-directing agents in metal oxide NCs,[22] exemplified in the fluorinated synthesis of TiO_2 NCs,[51,52] F doped F:In_2O_3,[7] and Sn codoped F,Sn:In_2O_3 NCs.[6] Metal fluoride precursors, such as SnF_4, decompose to form HF in the presence of oleic acid during the reaction, releasing fluoride anions and passivating the In-O surfaces with In–F bonds.[51] Walsh *et al.* previously determined through density functional theory (DFT) calculations that for bixbyite In_2O_3, relaxed {111} facets are energetically preferred over oxygen terminated {100} facets ($\gamma_{(111)} < \gamma_{(100)}$).[53] However, surface-passivation by F^- in metal oxide NCs can be expected to alter the energetic sequence of the facets: F^- passivation of the {100} facets results in surface energy inversion ($\gamma_{(111)} > \gamma_{(100)}$).[52] Correspondingly, F^- functions as a favorable {100} facet capping agent over {111} surfaces in the bixbyite In_2O_3 NCs, hindering In atomic layer growth at F^- terminated {100} surfaces. This directs the synthesis of well-defined F:In_2O_3 cube NCs as previously elucidated when sufficient F^- passivation occurs at the {100} facets.[7]

Observation through electron microscopy strongly indicates that F functions as a facet-directing agent in the synthesis of F,Sn:In_2O_3 NCs, and X-ray photoelectron spectroscopy (XPS) was used to further probe the presence of F on their surfaces [Figs. 1(c) and S5]. XPS is sensitive to surface composition, since the escape depth of photoelectrons is only a few nanometers.[54] The existence of F on the F,Sn:In_2O_3 NC surface is revealed by XPS spectra acquired in the In 3p and F 1s regions [Fig. 1(c)]. The intensity of the F 1s peak at 684.6 eV, flanked by the In 3p doublet peaks, is consistent as the fluorine precursor concentration is maintained at 5% SnF_4 in NC synthesis. As shown in Fig. S6, In $3d_{5/2}$ signal components are assignable to lattice In-O (444.3 eV), In-OH (445.0 eV), and In-F (445.8 eV) species.[7,55] O 1s signal components are assignable to lattice oxygen (530.0 eV), oxygen adjacent to oxygen vacancies, or other charged defects, such as $F_O^{\cdot}$ (531.0 eV), surface hydroxyl (531.8 eV), and carbonyl (533.1 eV) species, respectively.[7,55] The presence of Sn near the NC surface can also be observed through the Sn 3d XPS signal indicating the coexistence of Sn and F near the NC surface (Fig. S6). XPS characterization thus supports the adsorption of fluorine on the In_2O_3 NC surfaces, which is linked to the stability and prevalence of {100} facets in cube-shaped NCs.

The cube shape of F,Sn:In_2O_3 NCs can thus be rationalized through the shape control model demonstrated for halide-passivated NCs.[18,22] The {100} group facets become strongly passivated by F^- capping on the F,Sn:In_2O_3 cube NC surfaces when adequate SnF_4 fluoride precursor is present during the NC growth reaction. Fluorine terminated {100} surface exposure becomes favorable, minimizing total surface energy and resulting in well-defined cube-shaped NCs. Under Sn codoping, stable surface faceting is observed to continue to be prevalent in the range from 0% to 3% $Sn(ac)_4$ dopant precursor concentration as observed through XRD [Fig. 1(d)] through the prevalence of the (400) crystalline index indium oxide bixbyite peak for drop-casted NC samples. $Sn(ac)_4$ precursor concentration over 4% results in rounding of the cube shape until spherical morphology becomes dominantly observed in TEM and a weaker (400) diffraction peak is seen in XRD. This can be explicated by the difference in preferred surface energy in Sn-rich surfaces, as compared to pristine In_2O_3. Fluorine termination of SnO_2 surfaces is reported to cause preferential surface energy stabilization of {102} facets rather than stabilizing {100} surfaces.[56,57] Excessive Sn doping will make In_2O_3 surfaces prone to forming Sn-rich surfaces that more resemble the SnO_2 tetragonal rutile phase, as compared to cubic bixbyite In_2O_3,[58] leading to perturbed non-{100} facet fluorine terminated NC surface stabilization. Thus, the presence of Sn near the surface results in rounded cube NC morphologies at higher $Sn(ac)_4$ concentration (4%–5%) and spherical NC shapes at excessive Sn dopant incorporation (10%) as observed in Fig. 1(a).

NC dopant incorporation

As is prevalent in *n*-type doped metal oxide NC systems,[1,59] substitutional Sn and F dopants incorporated in In_2O_3 NCs can be charge compensated by free electrons. During codoping of Sn and F in the In_2O_3 lattice, Kröger-Vink defect equilibrium equations demonstrate that deliberate codoping may promote additional free carriers over a single dopant.[5] The added Sn cationic dopant allows additional free-carrier compensation beyond previously reported F-doped In_2O_3 NCs,[7] leading to LSPR tuning to higher frequency due to higher free carrier concentration within the NCs. Sn is a well-established cationic *n*-type dopant that induces high free electron concentration in tin doped indium oxide (Sn:In_2O_3) transparent conductive oxide films.[60,61] Substitutional F dopants incorporated in the NCs can also be charge compensated by free electrons. F is a similarly established anionic *n*-type dopant analog to Sn, inducing a high free electron concentration in fluorine doped tin oxide (F:SnO_2) transparent conductive oxide films.[60,61] A Kröger-Vink defect notation equation[62] demonstrates that deliberate In site substitution by Sn cations [Eq. (1)] and substitution on O sites by F anions [Eq. (2)] induce one free electron per site,[63,64]

$$(2Sn_{In} \cdot O_i)^x \rightarrow 2Sn_{In}^{\cdot} + \frac{1}{2}O_{2(g)} + 2e', \tag{1}$$

$$In_{In}^x + 3O_O^x \underset{InF_3}{\rightarrow} 2In_{In}^x + 3F_O^{\cdot} + \frac{3}{2}O_{2(g)} + 3e'. \tag{2}$$

It is expected that the extent of dopant incorporation will affect strain of the crystalline lattice. The impact on crystal lattice straining when F^- and Sn^{4+} are incorporated into In_2O_3 NCs is observed by analyzing XRD as a function of Sn incorporation. F,Sn:In_2O_3 NC [1%–12.5% $Sn(ac)_4$] XRD patterns confirm that the cubic bixbyite In_2O_3 crystal structure is well maintained throughout the Sn dopant range [Fig. 1(d)].[65] With the fluorine crystal ionic radius of F^- (1.19 Å) being smaller than that of O^{2-} (1.28 Å) in bixbyite phase In_2O_3,[66] lattice contraction is expected when fluorine occupies oxygen sites.[5,60] Since the Sn^{4+} (0.83 Å) ionic radius is smaller than In^{3+} (0.94 Å), Sn^{4+} cations substituting In^{3+} are also expected to cause lattice contraction to occur.

However, lattice expansion was observed instead of the expected lattice contraction due to F^- and Sn^{4+} incorporation when XRD peak shifts were analyzed through Rietveld refinement. XRD patterns revealed the displacements of the (222) reflections that correspond to lattice expansion induced by Sn^{4+} doping [Fig. 1(e)]. Through Vegard's law fitting, the y-intercept for F,Sn:In_2O_3 NC is at 10.164 Å, indicative of an expanded lattice constant when assuming F is present and Sn dopants are not present in the lattice for NCs with similar size, to exclude size effects (Fig. S7).[67] This is larger than the reported bulk In_2O_3 value of a = 10.119 Å,[68] with the expansion attributed to electrostatic repulsion of F ion dopants.[7] Lattice expansion is observed to occur in F,Sn:In_2O_3 NCs, similar to structural trends reported in F:SnO_2 and Sn:In_2O_3 films.[58,69] This expansion can be explained by electronic repulsion of doped impurity centers, as observed in bulk tin doped indium oxide by Frank and Köstlin[58] The observed trend indicates that at incremental doping levels, the high effective charge of the Sn ions causes a repulsion force that cannot be completely screened by the free electron gas.

F,Sn:In_2O_3 NC LSPR optical properties

LSPR spectral tuning is achieved by dopant incorporation control. Incremental addition of Sn results in the generation of free carriers [Eq. (1)], leading to higher free charge carrier concentration within the NCs.[70] With the naked eye, NC solvent dispersions are observably bluer in color as the Sn dopant concentration is increased [Fig. 2(a), bottom]. UV-Vis-NIR spectra show blue-shifting of LSPR extinction as the $Sn(ac)_4$ dopant precursor is increased [Fig. 2(a)]. At a high Sn dopant concentration [4%–15% $Sn(ac)_4$], the NC shape is progressively more spherical, leading to observation of a single mode LSPR peak characteristic of sphere shaped plasmonic nanoparticle ensembles. At a lower 0%–3% $Sn(ac)_4$ dopant concentration, a well-defined multimodal lineshape is observed arising from the cubic NC morphology.[7] The faceting effect of the F dopant in this low Sn dopant concentration window allows cube NC morphology to be retained while Sn is incrementally doped,

$$\epsilon_p = \epsilon_\infty - \frac{\omega_p^2}{\omega^2 + i\gamma\omega}, \tag{3}$$

$$\gamma = \gamma_L - \frac{\gamma_L - \gamma_H}{\pi}\left[\arctan\left(\frac{\omega - \gamma_X}{\gamma_W}\right) + \frac{\pi}{2}\right]. \tag{4}$$

The optical properties in plasmonic metal oxides are determined by the dielectric function [Eq. (3)]. It is often described by the Drude model for a collective free electron gas oscillation under an externally applied electromagnetic field. This depends on the bulk plasma frequency ω_p, which is a function of the free electron concentration n_e within the NCs, and the high frequency dielectric background ϵ_∞. This model has been broadly applied for $Sn{:}In_2O_3$.[15,70,71] The relation between plasma frequency and free electron concentration $\omega_p = \sqrt{\frac{n_e e^2}{\varepsilon_0 m^*}}$, where n_e is the free electron concentration, e is the elementary electronic charge, ε_0 is the permittivity of free space, and m^* is the effective mass, allows assessment of free carrier concentration within the NCs.[6,71] In the extended Drude model, an empirical frequency-dependent damping function [Eq. (4)] is used to model ionized impurity scattering of the free electrons.[72,73] Under the excitation of external electromagnetic waves with frequencies lower than the plasma frequency, oscillating free electrons are strongly influenced by screened ionized impurity scattering effectively akin to a direct current electrical field.[70] Ionized scattering centers include intrinsic divalent ionized oxygen vacancy donors[71] and substitutional monovalent dopant ions ($Sn^{\cdot}_{In}$ and $F^{\cdot}_{O}$) in the synthesized NCs,[6,70] leading to changes in γ_L low frequency damping. In the high-frequency regime and above the crossover frequency γ_X, the free electrons no longer interact as strongly with local ionized impurity centers, and damping levels off to a constant high frequency damping value, γ_H, due to reduced scattering probability at a higher oscillatory frequency.[70,74]

At higher Sn dopant concentrations, $F,Sn{:}In_2O_3$ NCs are nearly spherical, so their LSPR spectra were fit to a single peak using the extended Drude model. The experimentally collected spherical 10% $Sn(ac)_4$ NC spectrum was fitted using MATLAB, implementing the extended Drude model and a reduced square method used to extract the free carrier concentration determined by the plasma frequency

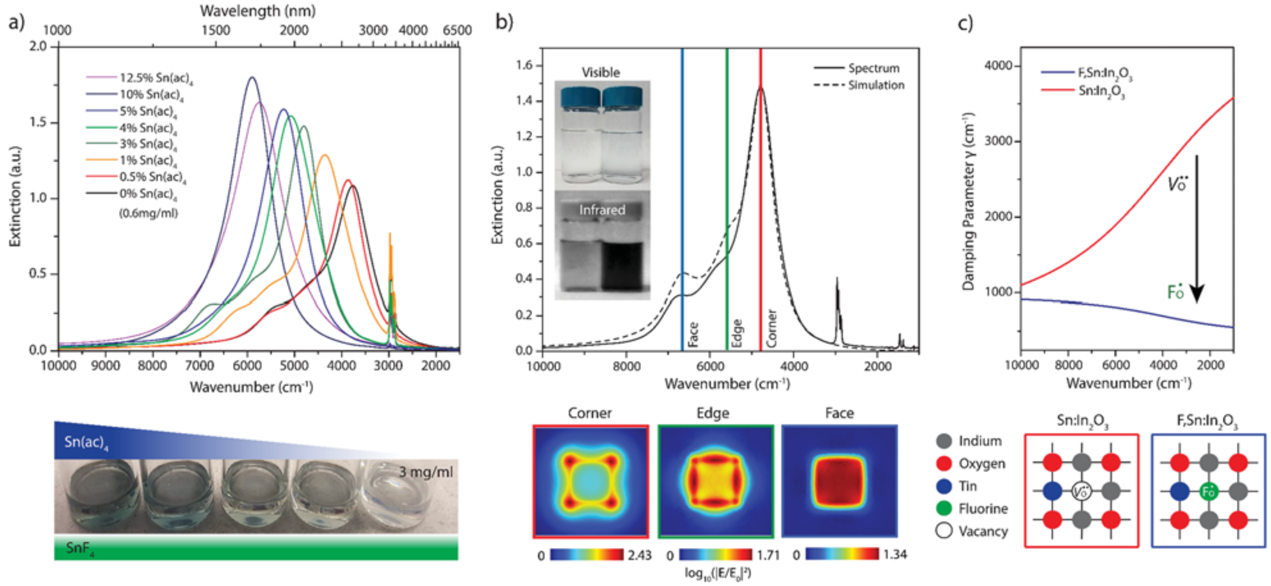

FIG. 2. (a) $F,Sn{:}In_2O_3$ NC UV-Vis-NIR/FTIR extinction spectra. Tunable blue-shifted LSPR response is observed as $Sn(ac)_4$ dopant concentration is increased, until the blue shift saturates beyond 10% $Sn(ac)_4$. (Bottom) Photograph of hexane dispersed $F,Sn{:}In_2O_3$ NCs (3 mg/ml) [0%–5% $Sn(ac)_4$, right to left]. (b) UV-vis-NIR/FTIR measured extinction spectrum (solid line) for $F,Sn{:}In_2O_3$ [3% $Sn(ac)_4$] NC cubes and simulated extinction spectrum (dotted line). (Inset) IR camera photograph of hexane at left, and dispersed $F,Sn{:}In_2O_3$ NC 3% $Sn(ac)_4$ (0.1 mg/ml) in hexane at right demonstrating strong, spectrally selective extinction in the IR. (Bottom) Near-field maps showing FEM simulated corner (left), edge (middle), and face (right) modes, with 4800 cm^{-1} corner, 5600 cm^{-1} edge, and 6600 cm^{-1} face centered eigenmodes, respectively. (c) Extended Drude model damping parameter extracted from extinction spectra for $F,Sn{:}In_2O_3$ 3% $Sn(ac)_4$ NC (blue) demonstrating low damping, benchmarked to damping parameters from $Sn{:}In_2O_3$ NC (red) at a similar plasma frequency. (Bottom) Schematic of F dopant monovalent ionized impurity occupying divalent oxygen vacancy center, reducing ionized impurity scattering in indium oxide.

Published under license by AIP Publishing

ω_p and impurity scattering-influenced frequency dependent damping parameters γ_H at high and γ_L at low frequencies.[75,76] Plasma frequency parameter extraction allowed the determination of a free carrier concentration of $n_e = 1.15 \times 10^{21}$ cm^{-3} in the NCs. The plasma frequency of $\omega_p = 17\,155$ cm^{-1} in this F,Sn:In_2O_3 NC sample is noticeably blue-shifted compared to previously reported highly doped Sn:In_2O_3 NCs at $\omega_p = 15\,841$ cm^{-1},[75] which is associated with anionic fluorine codoping affecting additional free carriers in F,Sn:In_2O_3 NCs.[6,7]

Shape induced LSPR modes become dominant in well-faceted cubic particles, with oscillatory near-field eigenmodes becoming apparent in corner-, edge-, and face-centered modes in each NC.[17] Spectral simulation was conducted with the finite element method (FEM) in the COMSOL wave design module inputting MATLAB extracted dielectric function parameters, reproducing the main absorption spectral feature of the spherical NCs (Fig. S8). For the multimodal extinction spectra in cubic shaped F,Sn:In_2O_3 NCs, simulations using the FEM based COMSOL wave design module were iteratively refined with the extended Drude model initial parameters from the MATLAB least squares method.[6,76] A simulated spectrum showing the three distinct LSPR modes induced by shape, comparable to the experimental extinction spectrum [Fig. 2(b)], was obtained for a F,Sn:In_2O_3 [3% Sn(ac)$_4$] NC. The main peak observed at 4750 cm^{-1} is attributed to the corner mode (red), 5600 cm^{-1} the edge mode (green), and 6600 cm^{-1} the face mode (blue). In F,Sn:In_2O_3 NCs synthesized using variable Sn dopant precursor levels, the free carrier concentrations are observed to increase with Sn dopant concentration until the observed blue-shifting saturates at the maximum observed value of $n_e = 1.32 \times 10^{21}$ cm^{-3} for 10% Sn(ac)$_4$ and red-shifts again for higher Sn dopant precursor concentrations (Table I). This demonstrates the viability of LSPR tuning in faceted NCs through synthetic dopant incorporation control, while the cubic shape is retained within the range of fluorine induced faceting effects.

The low-frequency damping parameter is substantially reduced by F codoping, leading to narrower LSPR modes as compared to only Sn doped In_2O_3 [Fig. 2(c)]. The damping function [Eq. (4)] incorporates the low frequency damping γ_L that reflects the strength of internal scattering of free electrons.[71,75] The scattering cross section in ionized impurity scattering is proportional to the square of the ionic charge (Z^2). Fluorine induced substitutional $F_O^{\cdot}$ defects, according to Eq. (2), reduce the concentration of divalent oxygen vacancies $V_O^{\cdot\cdot}$ and allow suppressed ionized impurity scattering to occur within the codoped F,Sn:In_2O_3 NCs [Fig. 2(c), bottom].[6,70] As compared to fluorine-free uniformly doped Sn:In_2O_3 NCs previously reported in the literature,[75] the damping parameter in fluorine-containing F,Sn:In_2O_3 [3% Sn(ac)$_4$] NCs is observed to be significantly lower with $\gamma_L = 585$ cm^{-1} [Fig. 2(c)]. Similarly, F,Sn:In_2O_3 NCs at various Sn dopant precursor levels consistently demonstrate reduced impurity scattering near $\gamma_L = 650$ cm^{-1} between 0% and 10% Sn(ac)$_4$ (Table S1). In uniformly doped Sn:In_2O_3 NCs, oxygen vacancies and neutral defect clusters $(Sn_{In}^{\cdot} - O''_i)^X$ cause noticeable ionized impurity scattering induced damping in the low frequency regime.[70,75] Previous work demonstrated that damping parameters in Sn:In_2O_3 NCs with surface segregated dopants approach those of oxygen vacancy ($V_O^{\cdot\cdot}$) doped In_2O_3 NCs, around 1000 cm^{-1},[58,77] which was lower than the reported damping in Sn:In_2O_3 NCs with uniformly distributed dopants. The damping parameter of fluorine incorporated F,Sn:In_2O_3 NCs is less than the reported values in these surface segregated Sn:In_2O_3 NCs, due to the suppression of $V_O^{\cdot\cdot}$ divalent oxygen vacancies with $F_O^{\cdot}$ monovalent ionized defect incorporation. This favorable reduction in ionized defect scattering enables high NC quality factor $Q = \frac{\omega_{LSPR}}{\kappa}$ (Table I), where narrow spectral linewidth κ and high energy LSPR peak frequency ω_{LSPR} are achieved.[78]

TABLE I. F,Sn:In_2O_3 NC [0%–12.5% Sn(ac)$_4$] dopant series LSPR spectral peak position (ω_{LSPR}), free carrier concentration (n_e), and NC quality factor (Q) values.

F,Sn:In_2O_3 NC	ω_{LSPR} (cm^{-1})	n_e (cm^{-3})	Q
0% Sn(ac)$_4$	3744	0.69×10^{21}	3.59
0.5% Sn(ac)$_4$	3845	0.74×10^{21}	4.04
1% Sn(ac)$_4$	4338	0.94×10^{21}	3.77
3% Sn(ac)$_4$	4789	1.15×10^{21}	5.22
4% Sn(ac)$_4$	5066	1.17×10^{21}	4.26
5% Sn(ac)$_4$	5216	1.25×10^{21}	2.65
10% Sn(ac)$_4$	5858	1.32×10^{21}	5.61
12.5% Sn(ac)$_4$	5737	1.26×10^{21}	4.33

Since F,Sn:In_2O_3 NCs exhibit narrow LSPR optical response, it is expected that they can create strong near-field enhancement (NFE) in the IR range. NFE is prominent in the near-field simulations, with intense electromagnetic hot-spots localized at the distinctive morphological features of the NC cube. NFE is observed in cubic F,Sn:In_2O_3 [3% Sn(ac)$_4$] NCs at the geometric corner, edge, and face-centered eigenmodes with NFE factor ($\log_{10}|E/E_o|^2$) values of 2.43, 1.71, and 1.34, respectively [Fig. 2(b), bottom]. At lower Sn dopant precursor levels, e.g., F,Sn:In_2O_3 [0% Sn(ac)$_4$] NCs, lower NFE factor values of 2.23, 1.57, and 1.21 are, respectively, obtained for corner, edge, and face modes (Fig. S9). In spherical F,Sn:In_2O_3 [10% Sn(ac)$_4$] NCs with a single LSPR mode, a comparatively low NFE value of 1.92 was obtained due to the absence of high-curvature sharp morphological corner features. To experimentally probe IR near-field effects in ensemble F,Sn:In_2O_3 NC structures, NCs were assembled to form nanocavity architecture arrays.

Monolayer F,Sn:In_2O_3 NC film assembly

Spectral tunability can be advantageously used in monolayer NC film array architectures, realizing tunable IR range near-field nanocavities between the NC arrays and substrate without being restricted by particle size dependent tuning.[11] Spectral LSPR tunability in solution dispersed NCs was achieved as discussed above through chemical Sn dopant incorporation control during colloidal synthesis. By assembling LSPR tuned F,Sn:In_2O_3 NC monolayer films on top of PbS QD monolayer films, self-assembled nanocavities can be fabricated, sandwiching PbS QD emitters between the substrate and LSPR active cube NC monolayers. To assemble a nanocavity layer over excitonic PbS QDs, a F,Sn:In_2O_3 cube NC monolayer is fabricated using a modified two-phase assembly method,[37,79] and NCs dispersed in an immiscible nonpolar hexane phase (1 mg/ml, 100 μl) were floated on top of a polar ethylene glycol phase [Figs. 3(a) and S10]. Separately, PbS QD monolayer films were fabricated from

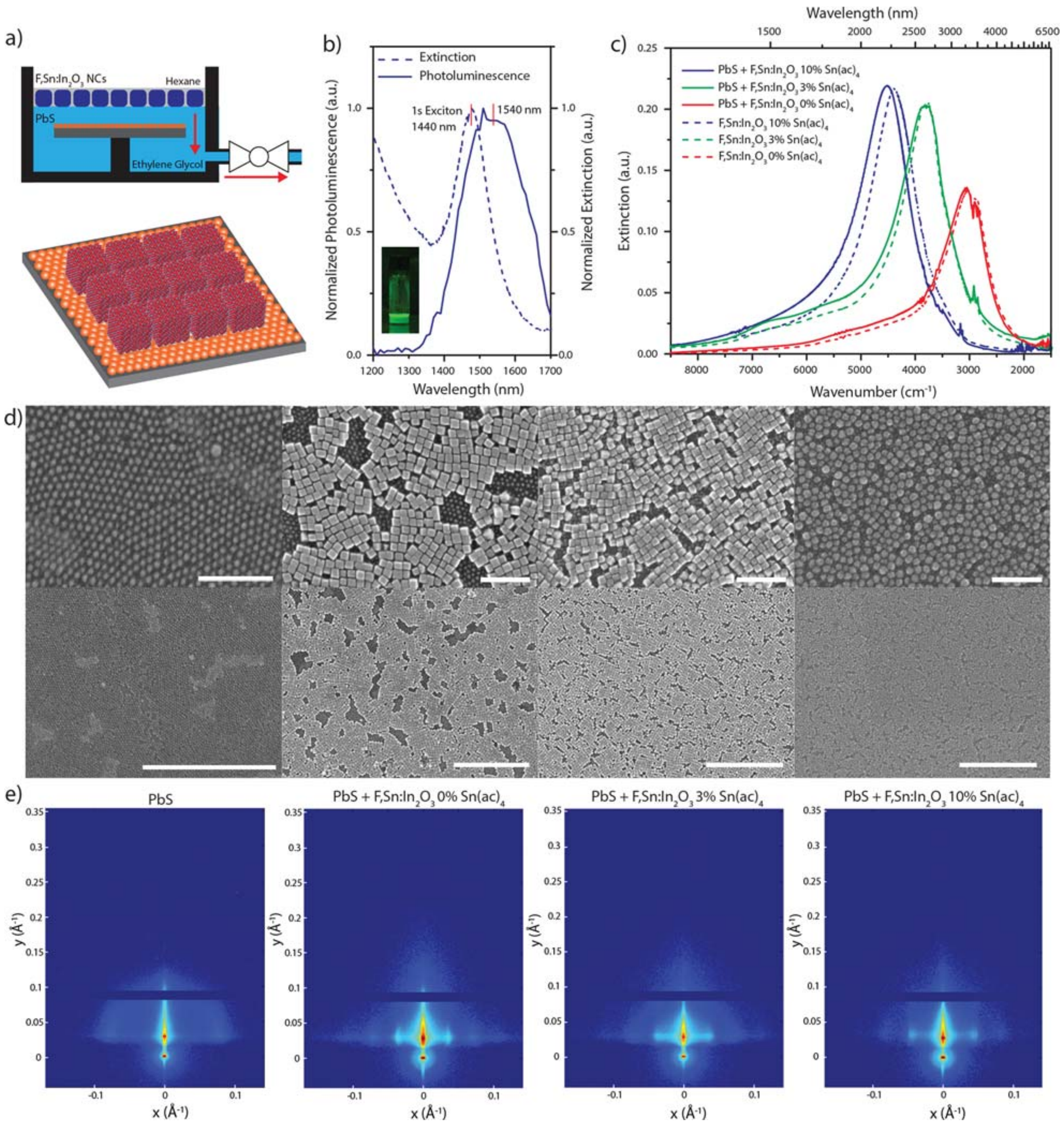

FIG. 3. (a) Liquid-air monolayer NC assembly schematic of Teflon trough, hexane dispersed F,Sn:In_2O_3 NCs on ethylene glycol, and spin-coated PbS QD substrate (top). Ethylene glycol is drained to place a monolayer F,Sn:In_2O_3 NC assembly on top of the PbS QD layer (bottom). (b) UV-Vis-NIR spectrum of 1s exciton absorption peak of PbS NCs (dotted) dispersed in tetrachloroethylene with 1540 nm PbS NC film photoluminescence (solid). IR photo (inset) shows photoemission of the PbS sample dispersed in hexane. (c) FTIR extinction spectrum of the F,Sn:In_2O_3 NC monolayer assembled film on a Si substrate (dotted) and the F,Sn:In_2O_3 NC monolayer film overlayered on the PbS QD film on a Si substrate (solid) exhibiting very similar extinction. (d) SEM images of PbS QD films, and F,Sn:In_2O_3 [0%, 3%, 10% $Sn(ac)_4$] NC monolayers over PbS NC films. Bars correspond to 100 nm (top). Wide field SEM images of the same films showing monolayer uniformity of film architecture. Bars correspond to 500 nm (bottom). (e) GISAXS of NC monolayer films on Si substrates for (far left) PbS QDs, (middle left) F,Sn:In_2O_3 cubes [0% $Sn(ac)_4$], (middle right) F,Sn:In_2O_3 cubes [3% $Sn(ac)_4$], and (far right) F,Sn:In_2O_3 [10% $Sn(ac)_4$] layered over PbS QD films. Monolayer NC cube arrays show first, second, and third order scattering peaks corresponding to regular NC packing in a planar array.

Published under license by AIP Publishing

a dilute hexane-octane dispersion (5 mg/ml) by spin-coating. The ethylene glycol subphase layer was drained through a connected ball valve near the bottom of the Teflon trough. This approach minimizes perturbation of the PbS QD layer and of the liquid-air interface assembled film that forms after hexane evaporates under a glass cover. Although it may also be possible to spincoat the top layer from a solvent that leaves the PbS QD layer in place, this alternative would require postsynthetic NC ligand stripping to transfer the NCs to a polar solvent.

In simulations, dopant controlled tunable LSPR nanocubes show NFE at well-defined morphological features. To experimentally probe an enhanced electromagnetic field due to F,Sn:In_2O_3 NC arrays, emission of PbS QD films is used as a probe. The dependence of the quantum transition rate of the emitters on nanocavity electromagnetic field intensity and the relationship between detuning frequencies of the LSPR cube array can be experimentally interrogated via plasmon-exciton coupling effects. PbS QDs are a direct bandgap semiconductor material with tunable IR photoemission influenced by size-dependent quantum confinement.[34,80] PbS QDs are synthesized to tune the 1s exciton peak position and correspondingly the PbS film photoluminescence peak frequency [Fig. 3(b)] toward longer wavelengths near the F,Sn:In_2O_3 cube NC cavity resonance.[34]

LSPR spectral tunability in self-assembled F,Sn:In_2O_3 NC monolayer films is characterized using UV-Vis-NIR spectroscopy [Fig. 3(c)]. The F,Sn:In_2O_3 and PbS composite film LSPR extinction feature is only modestly perturbed compared to the F,Sn:In_2O_3 NC only films. The F,Sn:In_2O_3 cube [0% Sn(ac)$_4$] monolayer assembly shows a nanocavity mode LSPR peak at ω_{cav} = 3030 cm^{-1}, F,Sn:In_2O_3 cube [3% Sn(ac)$_4$] at ω_{cav} = 3740 cm^{-1}, and F,Sn:In_2O_3 NC [10% Sn(ac)$_4$] at ω_{cav} = 4527 cm^{-1}. Monolayer NC film arrays show LSPR red-shifting due to interparticle plasmon coupling with adjacent NCs when compared with noninteracting TCE solution dispersed NCs. Monolayer F,Sn:In_2O_3 cube [0% Sn(ac)$_4$] arrays show LSPR peak shift of $\Delta\omega_{LSPR}$ = 714 cm^{-1}, F,Sn:In_2O_3 cube [3% Sn(ac)$_4$] of $\Delta\omega_{LSPR}$ = 1049 cm^{-1}, and F,Sn:In_2O_3 NC [10% Sn(ac)$_4$] of $\Delta\omega_{LSPR}$ = 1331 cm^{-1}. This trend is consistent with stronger redshift due to coupling for NCs with higher overall dopant concentration.[78] The interparticle plasmon coupling resulting in LSPR redshifting indicates that the NC arrays form a collective ensemble as a nanocavity that can be probed through PbS emissive lifetime measurement correlation.

SEM images of assembled films show the local ordering in F,Sn:In_2O_3 NC monolayers on PbS QDs, with micrometer range uniformity [Figs. 3(d) and S11]. The F,Sn:In_2O_3 NC cube [0%, 3% Sn(ac)$_4$] monolayers show planar cubic packing, while the F,Sn:In_2O_3 NC spheres [10% Sn(ac)$_4$] show monolayer hexagonal packing over the PbS QD layers. The PbS QD monolayer is maintained after the F,Sn:In_2O_3 cube NC monolayer film layer is deposited using the two-phase solution assembly method (Fig. S11). To further characterize the uniformity of the films, GISAXS was used to observe the ordering of layered F,Sn:In_2O_3 cubes and PbS QD films [Fig. 3(e)].[37,81] The scattering peaks for these composite F,Sn:In_2O_3 cubes and PbS QD films are consistent with regular particle spacing of the F,Sn:In_2O_3 NC cubes, with periodicity representing the interparticle NC center-to-center distance. For F,Sn:In_2O_3 cubes [0% Sn(ac)$_4$], the periodicity is measured as a = 17.2 ± 0.3 nm with scattering peaks consistent with the first, second, and third order in-plane peaks. Higher Sn doped F,Sn:In_2O_3 cubes [3% Sn(ac)$_4$] are observed to have a = 16.7 ± 0.1 nm with a similar planar array structure. For the F,Sn:In_2O_3 NCs [10% Sn(ac)$_4$], periodicity is measured as a = 13.4 ± 0.1 nm with scattering peaks consistent with first, second, and third order (Fig. S12). The interparticle distances and structures of F,Sn:In_2O_3 NC layers on top of PbS QD films are the same as F,Sn:In_2O_3 only monolayer film arrays. For example, a pristine F,Sn:In_2O_3 cube [0% Sn(ac)$_4$] monolayer array is observed to have interparticle distance of a = 17.5 ± 0.1 nm with apparent first, second, and third order scattering peaks, which is nearly identical to the structure of a NC cube array overlayered on a PbS QD film. Similar results were also observed for other pristine films, with F,Sn:In_2O_3 cube NC [3% Sn(ac)$_4$] interparticle distance at a = 16.8 ± 0.3 nm and F,Sn:In_2O_3 NC [10% Sn(ac)$_4$] films at a = 13.2 ± 0.4 nm. In a pristine PbS QD film, an interparticle distance of a = 8.1 nm is observed. GISAXS reveals that the F,Sn:In_2O_3 NC cube monolayer films' local architecture observed through SEM is sufficiently uniform over a wide area for nanocavity spectral characterization.

Plasmon-exciton coupling and nanocavity effects

F,Sn:In_2O_3 cube NCs exhibit IR range LSPR tunability, and simulations predict they will create emergent NFE. These properties can be leveraged to realize dopant induced spectrally tunable IR nanocavities in monolayer film architectures, which has been difficult to access using materials such as Ag or Au noble metal nanoparticles that have high, fixed free carrier concentrations. By placing a PbS QD layer under LSPR active F,Sn:In_2O_3 NC monolayers, QDs can be used to realize exciton-plasmon coupling and to act as photoluminescent probes to understand tunable IR near-field nanocavities.[41] The photoluminescence decay lifetime (τ_0) is representative of the population relaxation rate from the exciton to the ground state, i.e., hole-electron pair recombination, in PbS QDs. Coupling the LSPR induced enhanced near-field with photoluminescent exciton recombination ($\mathit{\Gamma}_0 = \frac{1}{\tau_0}$) leads to accelerated lifetime decay rate ($\mathit{\Gamma}_{tot} = \frac{1}{\tau_{tot}} = \mathit{\Gamma}_0 + \mathit{\Gamma}_{cav}$),[82,83]

$$\mathit{\Gamma}_{cav} = \left(\frac{4g^2}{\kappa}\right)\frac{1}{1+\left(\frac{2\delta}{\kappa}\right)^2} = \Gamma_{tot} - \mathit{\Gamma}_0, \tag{5}$$

$$g = \frac{1}{2}\sqrt{(\mathit{\Gamma}_{tot} - \mathit{\Gamma}_0)\left(1+\left(\frac{2\delta}{\kappa}\right)^2\right)\kappa}. \tag{6}$$

The modulation of electromagnetic field in a confined cavity exerts an influence by enhancing the excited state to ground state transition rate ($\mathit{\Gamma}_{cav}$) according to Fermi's golden rule, which can be reiterated into the Purcell effect. The coupling strength can be extracted from the experimental photoluminescence lifetime decay rate using Eq. (5). The off-resonance frequency between the plasmonic nanocube monolayer cavity (ω_{cav}), with LSPR cavity linewidth κ, and QD emitter (ω_{emit}) is termed detuning frequency ($\delta = \omega_{cav} - \omega_{emit}$).[82] To assess the interaction strength between LSPR and excitons, Eq. (5) can be reorganized to give coupling strength (g) in Eq. (6).[82,84] Controlled dopant incorporation into NCs is advantageous as LSPR frequency can be tuned in the IR, without relying on size induced tuning as in Ag or Au nanoparticles.

Empirical coupling strength is assessed through IR photoluminescence lifetime measurement with stretched exponential decay curve fitting.[41] A layered assembly of F,Sn:In$_2$O$_3$ cube NCs [3% Sn(ac)$_4$] on a PbS QD film was observed to have a shortened lifetime of $\tau_0 = 0.016$ ns as compared to a PbS-only film at $\tau_0 = 0.365$ ns [Fig. 4(a)]. For reference, a PbS quantum film ($\omega_{emit} = 6944$ cm^{-1}) overlayed by highly off-resonant F,Sn:In$_2$O$_3$ [0% Sn(ac)$_4$] NC cubes ($\omega_{cav} = 3051$ cm^{-1}, $\kappa = 28.8$ THz) showed little evidence of coupling. The lifetime decay was only weakly enhanced, giving $g = 0.99$ THz (4.09 meV), indicating limited coupling behavior under high detuning frequency ($\delta = 3893$ cm^{-1}). In the case of closer spectral overlap between the LSPR nanocavity and excitonic QD emitters, the F,Sn:In$_2$O$_3$ [3% Sn(ac)$_4$] NC cube monolayer ($\omega_{cav} = 3808$ cm^{-1}, $\kappa = 32.7$ THz) showed enhanced exciton lifetime decay with a coupling strength of $g = 4.08$ GHz (16.85 meV) at $\delta = 3136$ cm^{-1}. In a sample wherein PbS QDs are coupled to a film of spherical F,Sn:In$_2$O$_3$ [10% Sn(ac)$_4$] NCs ($\omega_{cav} = 4521$ cm^{-1}, $\kappa = 33.3$ THz), despite a lower detuning frequency at $\delta = 2423$ cm^{-1} and closer resonant overlap, the coupling strength was observed to be noticeably reduced at $g = 1.40$ THz (5.78 meV). This is due to spherical shaped NCs having

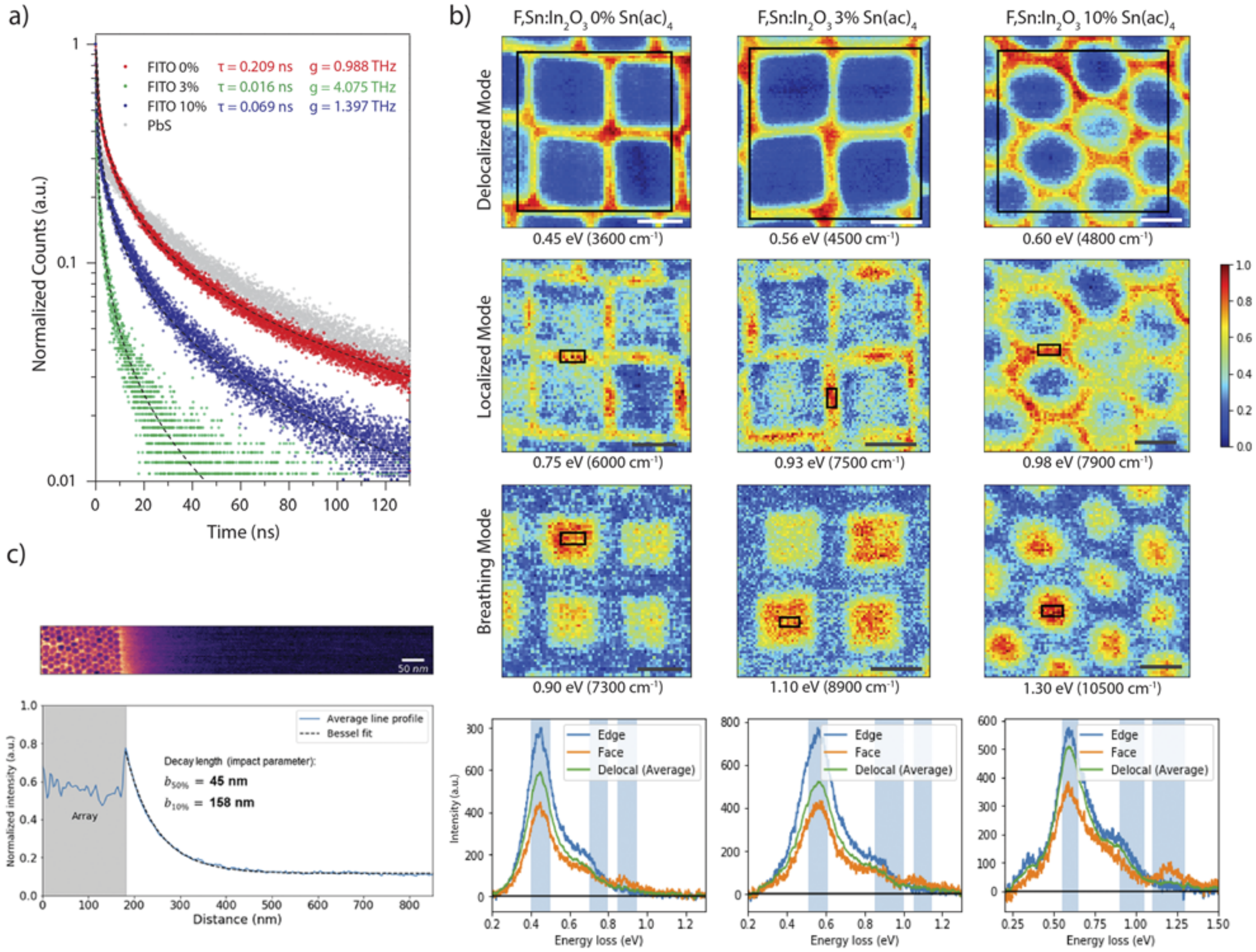

FIG. 4. (a) Photoluminescence lifetime measurement of PbS QD films coupled with F,Sn:In$_2$O$_3$ NC monolayer assembly nanocavities. Enhanced decay lifetime is observed when LSPR active F,Sn:In$_2$O$_3$ NC cubes are present. (Red) PbS QDs coupled to a detuned F,Sn:In$_2$O$_3$ [0% Sn(ac)$_4$] NC cube monolayer exhibit weak decay enhancement behavior, while those (green) coupled to a F,Sn:In$_2$O$_3$ [3% Sn(ac)$_4$] NC cube monolayer demonstrate high Purcell enhancement. (Blue) PbS QDs coupled to spherical F,Sn:In$_2$O$_3$ [10% Sn(ac)$_4$] NCs show intermediate decay rates. The laser excitation wavelength was 850 nm, exciting across the PbS bandgap, at 25 μW intensity and 5 MHz repetition rate. (b) STEM-EELS maps of F,Sn:In$_2$O$_3$ NC arrays. Columns represent (left) F,Sn:In$_2$O$_3$ [0% Sn(ac)$_4$] NC cube, (middle) F,Sn:In$_2$O$_3$ [3% Sn(ac)$_4$] NC cube, and (right) F,Sn:In$_2$O$_3$ [10% Sn(ac)$_4$] NC sphere arrays, with intensity maps normalized to the observed mode. Distinct spatially delocalized, interparticle gap edge localized, and NC localized face breathing modes are observed at the respective labeled frequencies. Scale bars are 5 nm. (Bottom) EELS spectra demonstrate near-field tunability observed in the delocalized average mode, localized gap edge, and face breathing mode in a demarcated reduced map area for the respective F,Sn:In$_2$O$_3$ NC arrays. (c) STEM-EELS map of F,Sn:In$_2$O$_3$ [0% Sn(ac)$_4$] NC cube assembly array edge. A modified Bessel function of the second kind curve fit of the linear intensity profile shows the observation of delocalized LSPR 50% decay length impact parameter of 45 nm and 10% decay length impact parameter of 158 nm. Scale bar is 50 nm.

less NFE as compared to cube shaped NCs, later to be discussed in NC array simulations. The narrow cavity linewidth κ being in the 30 THz range for all monolayer film assemblies [Fig. 3(c)] is representative of the photonic mode decay rate, affirming that the IR nanocavity architecture is in the weak coupling regime by comparing the coupling strength to cavity linewidth ($g < \kappa$).[84–86] The localized photonic mode in the cavity decays faster than the exciton to LSPR coupled oscillation[87] leading to enhancement of the accessible pathway in photonic modes of decay and thus enhanced exciton photoluminescence decay rate induced by F,Sn:In_2O_3 NCs.

To further address the nanoscopic localized nature of F,Sn:In_2O_3 NC cube electromagnetic field coupling to PbS QD excitons, the Purcell enhancement[88] in Eq. (7) is evaluated with assistance from simulation models and direct STEM-EELS observations. In free space, unperturbed by the local electromagnetic field environment, spontaneous emission can be expressed by Eq. (8).[89] From Fermi's golden rule, the hole-electron pair recombination rate can be perturbed by the local electromagnetic field in a photonic cavity environment. This interaction is described in Eq. (9) as a time-independent term expressed by the enhanced local electromagnetic field (E) and exciton transition dipole moment (μ_{12}),[83,90]

$$F_p = \frac{\Gamma_{tot}}{\Gamma_0}, \tag{7}$$

$$\Gamma_0 = \frac{{\omega_0}^3 {\mu_{12}}^2}{3\pi\varepsilon_0 \hbar c^3}, \tag{8}$$

$$\Gamma_{tot} = \frac{2\pi}{\hbar^2}|\langle f|\mathrm{d}\cdot \mathrm{E}|i\rangle|^2 \rho(\omega_0) = \frac{2\pi}{\hbar^2}|\langle \mu_{12}E\rangle|^2 \rho(\omega_0). \tag{9}$$

The nanocube morphology of infrared LSPR active F,Sn:In_2O_3 NCs allows intense near-field localized resonance, allowing confinement of light beyond the diffraction limit. In a monolayer assembly array of cubes, the near-field enhancement effect is used to localize a high density of IR range light around the PbS QD array in a nanocavity.[26,41] Whereas photonic modes in free space would be broadly distributed over a wide frequency range, the infrared LSPR active F,Sn:In_2O_3 NCs allow photonic modes to be localized near a controllably tuned resonant frequency. The photonic density of states [$\rho(\omega_0)$] in a nanocavity is confined and centered around an LSPR resonance frequency (ω_{cav}) of quality factor $Q = \frac{\omega_{cav}}{\kappa}$, expressed as a Lorentzian distribution [Eq. (10)] corresponding to the experimentally observed LSPR cavity extinction spectra. The confined cavity electromagnetic field (E) is expressed as below and related to a normalized mode volume (V) in Eq. (11) for a nanocavity architecture,[89,91,92]

$$\rho(\omega_0) = \frac{2}{\pi\kappa}\frac{\left(\frac{\kappa}{2}\right)^2}{\left(\frac{\kappa}{2}\right)^2 + (\omega_{cav} - \omega_{emit})^2}, \tag{10}$$

$$|\langle \mu_{12}E\rangle|^2 = \frac{{\mu_{12}}^2 \hbar\omega_0}{2\varepsilon_0 n^2 V}\xi^2. \tag{11}$$

Intraband energy dissipation losses commonly observed in Au and Ag nanocavities can be advantageously avoided in the doped metal oxide nanocavity system. The IR range LSPR is well separated in frequency from band edge loss features, which are located in the near UV spectral range.[91,93] Therefore, emitter to cavity detuning components can be incorporated in Eq. (12) to fully describe the Purcell enhancement factor F_p. To account for the assumed random isotropic orientation between the exciton dipole of spherical QDs in a cavity, a ξ^2 dipole orientation factor of 1/3 is included in the Purcell factor expression. The nanocavity confinement of electromagnetic field modifies the mode volume (V) in Eq. (13), which is a pure electromagnetic property describing the effectiveness of the nanocavity in concentrating the electromagnetic field in confined space.[90,94] The local relative field amplitude of the cavity mode expressed as $\boldsymbol{E}$ is normalized so that the norm is unity at the maximum amplitude antinode of the incident electric field (E_0),[90,91]

$$F_p = \frac{3}{4\pi^2}\left(\frac{\lambda_0}{n}\right)^3\left(\frac{Q}{V}\right)\frac{\left(\frac{\kappa}{2}\right)^2}{\left(\frac{\kappa}{2}\right)^2 + (\omega_{cav} - \omega_{emit})^2}\xi^2, \tag{12}$$

$$V = \frac{1}{\varepsilon_0 n^2}\int \varepsilon(r)|\boldsymbol{E}(r)|^2 d^3 r. \tag{13}$$

STEM-EELS allows direct observation and verification of energy loss signatures associated with the spectrally tunable near-field existing in the assembled NC cube arrays [Fig. 4(b)]. Near-field intensity was simulated for the interparticle nanocube facet gaps. The emergent delocalized nature of near-field modes was directly observed. Near-field intensity in array assemblies is observed to be stronger compared to a single particle in both simulations and STEM-EELS measurement. In single particle F,Sn:In_2O_3 [10% Sn(ac)$_4$] STEM-EELS, a near-field energy loss peak located at 0.8 eV is weak (Fig. S14), while an eleven-fold near-field intensity increase was observed in the energy loss peak located at 0.6 eV for assembled NC gaps (Fig. S14). The interparticle NC array gap near-field shows higher NFE factor ($\log_{10}|E/E_o|^2$) values of 2.35 [Fig. 5(a)], while a single NC shows NFE factor of 1.92 (Fig. S9). A secondary higher energy mode centered at 0.98 eV emerges from STEM-EELS mapping in NC film arrays that is attributable to a localized gap confined near-field mode [Fig. 4(b)], while map profiles show that the main peak mode centered at 0.6 eV is a delocalized near-field ensemble mode. These maps in Fig. 4(b) show elastic scattering contrast due to a relatively significant portion of the electron beam undergoing high angle scattering when positioned on the particles. Hence, while less signal appears to be present when inspecting the map for the delocalized mode, this plasmon is essentially uniform in intensity across the entire ensemble. Figure S15 shows this by comparing the zero loss peak map with this delocalized map. The F,Sn:In_2O_3 NC monolayer film series observed by STEM-EELS demonstrates that the near-field is spectrally tunable, noticeable by the blue-shift in the primary energy loss at higher Sn dopant concentration, while the localized secondary mode is also observed in all three F,Sn:In_2O_3 NC assemblies [Figs. 4(b) and S15]. A high energy breathing mode was observed localized within the NC volume, which is a nonradiative dark mode that evades light scattering due to a symmetrical zero net dipole moment, but is exclusively observed through EELS.[42,95] Through STEM-EELS, long-range plasmonic near-field decay is directly observed at the edge of the nanocube assembly [Fig. 4(c)]. Simulated NFE factor values of 2.12 in F,Sn:In_2O_3 [0% Sn(ac)$_4$] NC arrays and 2.09 in F,Sn:In_2O_3 [3% Sn(ac)$_4$] NC arrays were derived for the interparticle nanocube gaps [Fig. 5(a)]. Secondary localized modes experimentally observed through STEM-EELS were

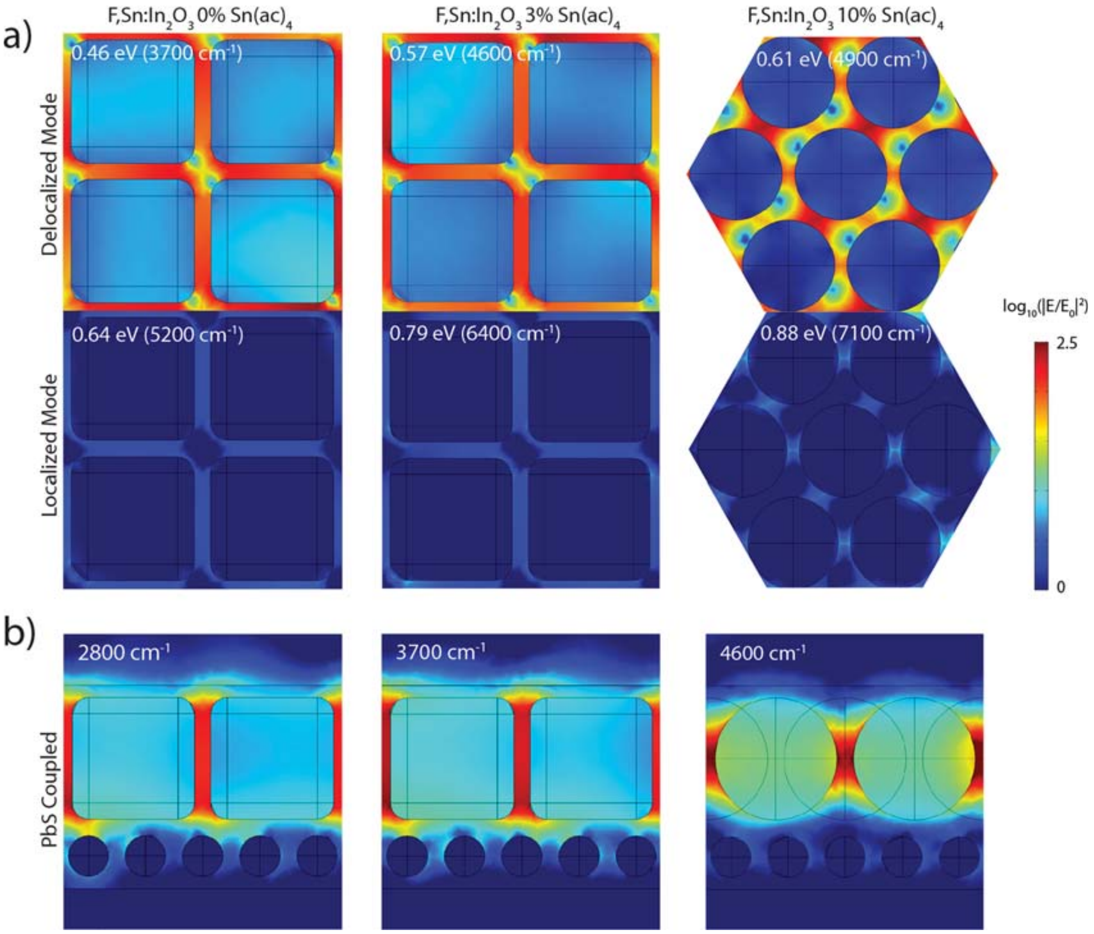

FIG. 5. (a) Simulated local NFE maps of F,Sn:In_2O_3 NC assemblies. Top-down view of F,Sn:In_2O_3 NC arrays and interparticle gaps simulating STEM-EELS environmental configuration without coupling to PbS QDs. Delocalized (top) and localized (middle) mode NFE maps at the respective frequencies, as observed through STEM-EELS. (b) Cross section NFE maps of coupled nanocavity assemblies, with PbS QDs coupled between the substrate and F,Sn:In_2O_3 NC array. Columns represent (left) F,Sn:In_2O_3 [0% $Sn(ac)_4$] NC cube, (middle) F,Sn:In_2O_3 [3% $Sn(ac)_4$] NC cube, and (right) F,Sn:In_2O_3 [10% $Sn(ac)_4$] NC sphere arrays.

simulated, with NFE factor values of 0.34 between the cube facet gaps in F,Sn:In_2O_3 [0% $Sn(ac)_4$] NC arrays, 0.36 in F,Sn:In_2O_3 [3% $Sn(ac)_4$] NC arrays, and 0.68 in F,Sn:In_2O_3 [10% $Sn(ac)_4$] NC arrays.

The collective electromagnetic mode volume in spectrally tuned NC films is correlated and quantified with the above Purcell effect lifetime decay enhancement measurements. The assembled cube array nanocavity local electromagnetic field intensity predicted through FEM simulation [Fig. 5(b)] is used to quantify the near-field enhanced electromagnetic field (E) from incident excitation (E_0).[91–93,96] With the PbS QD emitters (ω_{emit} = 6944 cm^{-1}, λ = 1540 nm) coupled to a F,Sn:In_2O_3 [3% $Sn(ac)_4$] cube NC cavity (Q = 3.49), the components of Eq. (12) can be evaluated. With locally enhanced electromagnetic near-field simulations under E_0 = 0.125 V m^{-1} incident intensity from the 25 μW excitation source ($I = \frac{cn\varepsilon_0}{2}|E_0|^2$), the delocalized photonic mode volume of the F,Sn:In_2O_3 NC array can be extracted. With the PbS QDs placed in the gap cavity between a cube array and the substrate, excitonic QDs experience an averaged near-field enhancement of E/E_0 = 1.30 [Fig. 5(b)]. With the coupled energy exchange between the plasmon and exciton, electromagnetic waves may migrate ballistically at a surface plasmon resonance over micrometer length scale.[97] The electromagnetic wave can be planarly confined in the nanocavity gap between the NC array and substrate, giving rise to a characteristic photonic mode volume.[98,99] The ensemble photonic cavity mode can be estimated [Eq. (13)],[100] and the delocalized nanocube mode volume for F,Sn:In_2O_3 [3% $Sn(ac)_4$] NCs corresponds to a 49 × 49 nm^2 LSPR-exciton coupled real-space delocalization range.[97] The further detuned F,Sn:In_2O_3 [0% $Sn(ac)_4$] NCs with E/E_0 = 1.35 had a 117 × 117 nm^2 delocalization range, when a nanocavity thickness of 10 nm is assumed for each case. For the spherical F,Sn:In_2O_3 [10% $Sn(ac)_4$] NC nanocavity (Q = 4.07), a lower NFE enhancement of E/E_0 = 1.03 was simulated and the delocalized NC cavity array is calculated to have 76 × 76 nm^2 real-space delocalization range. This explains the observed differences of the LSPR energy in FTIR extinction spectra between solution dispersed F,Sn:In_2O_3 NCs and the red-shifted spectra of the monolayer film assemblies. Through the photoluminescence lifetime analysis, the local near-field environment was probed to quantify the delocalized photonic cavity environment in the monolayer film architectures. The existence of near-field delocalization in a NC array was directly observed at the edge of the assembly through STEM-EELS. The intensity of the plasmonic near-field decays exponentially with a decay length of 113 nm [Figs. 4(c) and S14] as compared to a single particle characteristic decay length of only 9.1 nm. This dramatic difference further supports that the near-field cavity is not individually confined around each NC, but an ensemble collective behavior is existent in the nanoassembly array leading to a delocalized nanocavity mode volume with an optical effect that is readily apparent through exciton lifetime correlations.

CONCLUSION

Sn codoping allows LSPR spectral tunability to be achieved in cubic faceted F-doped In_2O_3 NCs. The F dopant plays a role in selectively passivating {100} crystallographic facet surfaces of In_2O_3, while addition of a Sn codopant precursor creates a synthetic handle for controlling LSPR tunability. In these colloidally synthesized F,Sn:In_2O_3 NC cubes, shape-dependent LSPR multimodal extinction features arise at the well-defined corners, edges, and faces of the NCs. Near-field enhancement effects arise at these morphological features while retaining spectral tunability. The dopant-induced, size-independent spectral LSPR tunability observed in solution dispersed F,Sn:In_2O_3 NCs can be further exploited in self-assembled films. The tunable near-field effect can be leveraged and enhanced by fabricating dense plasmonic nanocavity arrays in long-range ordered monolayer architectures, prepared by a liquid-air interface assembly. IR range photoluminescent PbS QDs were coupled with the LSPR near-field tunable F,Sn:In_2O_3 NC nanocavity structure, inducing plasmon-exciton coupling. By controlling the detuning frequency between PbS QD emitters and LSPR active F,Sn:In_2O_3 NC nanocavities, variable Purcell enhancement of the exciton decay rate was observed. To further understand the spatial near-field nature of assembled NC arrays, direct observations of LSPR near-field spatial distributions were made by monochromated STEM-EELS mapping. An intense localized near-field was observed between F,Sn:In_2O_3 NCs in the interparticle gap arrays, while ensemble plasmonic behavior was emergent. Extensive LSPR delocalization was apparent within and at the edge of F,Sn:In_2O_3 NC array assemblies, which creates a delocalized collective mode volume as supported by Purcell enhancement analysis.

F,Sn:In_2O_3 NC nanocubes induce a strong LSPR near-field response in the IR range, a property that can be further amplified by creating spatially dense and tunable nanocavity arrays, without relying on size dependent tuning as in conventional Ag and Au noble metal nanomaterials. The optical properties observed in F,Sn:In_2O_3 NCs have the potential to be harnessed in photocatalytic applications,[101] ultrafast photonic switching,[41] and plasmonic molecular sensors.[102] Coupling excitonic photoemission and LSPR near-field enhancement, derived from QD and plasmonic material classes of particles, respectively, can enable photonic "assembly of light" toward hybrid forms of light-matter interaction.[85] By synthetically tuning LSPR across an extended IR spectral range, faceted NCs with enhanced near-fields may have potential for coupling to low-energy elementary excitations beyond excitons found only in the IR range. These may include phonons,[103] polarons,[104] polaritons,[105] and molecular vibrations,[106] which were previously hard to approach with conventional noble metal classes of plasmonic nanostructures. The extended synthetic tunability of LSPR in doped metal oxide NCs, including F,Sn:In_2O_3 nanocubes, may enable this class of materials to unlock previously unrealized LSPR coupled light-matter interactions and phenomena.

SUPPLEMENTARY MATERIAL

See the supplementary material for additional information regarding NC sample SEM, EDX, XPS, XRD, and UV-Vis-NIR characterization methods, extended Drude parameters, and FEM simulated NFE. Additional NC film SEM, SAXS, FEM simulated NFE, and STEM-EELS characterization results are included.

ACKNOWLEDGMENTS

S.H.C., S.G., L.C.R., S.H., K.K., J.C., J.N., B.A.K., X.L., and D.J.M. acknowledge the support from the National Science Foundation (NSF, Grant Nos. CHE-1609656, CBET-1704634, NASCENT, an NSF ERC EEC-1160494, and CDCM, an NSF MRSEC DMR-1720595), the Welch Foundation (Grant Nos. F-1848, F-1464, and F-1662), and the Fulbright Program (Grant No. IIE-15151071). We are thankful to K. Jarvis, A. Dolocan, and H. Celio in the Texas Materials Institute (TMI) for user facility assistance. This work utilized the SAXS instrument acquired under an NSF MRI grant (Grant No. CBET-1624659). Some microscopy research was performed as part of a user proposal at the Oak Ridge National Laboratory (ORNL), the Center for Nanophase Materials Sciences (CNMS), which is a U.S. Department of Energy, Office of Science User Facility (J.A.H.), and by the U.S. Department of Energy, Office of Science, Basic Energy Sciences, Materials Science and Engineering Division (K.M.R.). This research was conducted, in part, using instrumentation within ORNL's Materials Characterization Core provided by UT-Battelle, LLC, under Contract No. DE-AC05-00OR22725 with the DOE, and sponsored by the Laboratory Directed Research and Development Program of Oak Ridge National Laboratory, managed by UT-Battelle, LLC, for the U.S. Department of Energy. L.C.R. acknowledges the MMRRSA School at ORNL. C.K.D. and J.H. acknowledge support from the Air Force Office of Scientific Research under Contract No. FA9550-15RYCOR159.

The authors declare no competing financial interest.

REFERENCES

[1] A. Agrawal, S. H. Cho, O. Zandi, S. Ghosh, R. W. Johns, and D. J. Milliron, "Localized surface plasmon resonance in semiconductor nanocrystals," Chem. Rev. **118**, 3121 (2018).

[2] M. Kanehara, H. Koike, T. Yoshinaga, and T. Teranishi, "Indium tin oxide nanoparticles with compositionally tunable surface plasmon resonance frequencies in the near-IR region," J. Am. Chem. Soc. **131**(49), 17736–17737 (2009).

[3] R. Buonsanti, A. Llordes, S. Aloni, B. A. Helms, and D. J. Milliron, "Tunable infrared absorption and visible transparency of colloidal aluminum-doped zinc oxide nanocrystals," Nano Lett. **11**, 4706–4710 (2011).

Published under license by AIP Publishing

[4] T. R. Gordon, T. Paik, D. R. Klein, G. V. Naik, H. Caglayan, A. Boltasseva, and C. B. Murray, "Shape-dependent plasmonic response and directed self-assembly in a new semiconductor building block, indium-doped cadmium oxide (ICO)," Nano Lett. **13**(6), 2857–2863 (2013).

[5] X. Ye, J. Fei, B. T. Diroll, T. Paik, and C. B. Murray, "Expanding the spectral tunability of plasmonic resonances in doped metal-oxide nanocrystals through cooperative cation–anion codoping," J. Am. Chem. Soc. **136**(33), 11680–11686 (2014).

[6] A. Agrawal, A. Singh, S. Yazdi, A. Singh, G. K. Ong, K. Bustillo, R. W. Johns, E. Ringe, and D. J. Milliron, "Resonant coupling between molecular vibrations and localized surface plasmon resonance of faceted metal oxide nanocrystals," Nano Lett. **17**(4), 2611–2620 (2017).

[7] S. H. Cho, S. Ghosh, Z. J. Berkson, J. A. Hachtel, J. Shi, X. Zhao, L. C. Reimnitz, C. J. Dahlman, Y. Ho, A. Yang *et al.*, "Syntheses of colloidal F:In_2O_3 cubes: Fluorine-induced faceting and infrared plasmonic response," Chem. Mater. **31**(7), 2661–2676 (2019).

[8] M. M. Alvarez, J. T. Khoury, T. G. Schaaff, M. N. Shafigullin, I. Vezmar, and R. L. Whetten, "Optical absorption spectra of nanocrystal gold molecules," J. Phys. Chem. B **101**(19), 3706–3712 (1997).

[9] G. V. Naik, V. M. Shalaev, and A. Boltasseva, "Alternative plasmonic materials: Beyond gold and silver," Adv. Mater. **25**(24), 3264–3294 (2013).

[10] S. A. Maier, *Plasmonics: Fundamentals and Applications* (Springer US, 2007).

[11] E. Ringe, M. R. Langille, K. Sohn, J. Zhang, J. Huang, C. A. Mirkin, R. P. Van Duyne, and L. D. Marks, "Plasmon length: A universal parameter to describe size effects in gold nanoparticles," J. Phys. Chem. Lett. **3**(11), 1479–1483 (2012).

[12] J. M. Luther, P. K. Jain, T. Ewers, and A. P. Alivisatos, "Localized surface plasmon resonances arising from free carriers in doped quantum dots," Nat. Mater. **10**, 361–366 (2011).

[13] A. Agrawal, I. Kriegel, and D. J. Milliron, "Shape-dependent field enhancement and plasmon resonance of oxide nanocrystals," J. Phys. Chem. C **119**(11), 6227–6238 (2015).

[14] S. Link and M. A. El-Sayed, "Size and temperature dependence of the plasmon absorption of colloidal gold nanoparticles," J. Phys. Chem. B **103**(21), 4212–4217 (1999).

[15] R. J. Mendelsberg, G. Garcia, and D. J. Milliron, "Extracting reliable electronic properties from transmission spectra of indium tin oxide thin films and nanocrystal films by careful application of the Drude theory," J. Appl. Phys. **111**(6), 063515 (2012).

[16] Y. Xia, X. Xia, and H.-C. Peng, "Shape-controlled synthesis of colloidal metal nanocrystals: Thermodynamic versus kinetic products," J. Am. Chem. Soc. **137**(25), 7947–7966 (2015).

[17] O. Nicoletti, F. de la Peña, R. K. Leary, D. J. Holland, C. Ducati, and P. A. Midgley, "Three-dimensional imaging of localized surface plasmon resonances of metal nanoparticles," Nature **502**(7469), 80–84 (2013).

[18] X. Xia, S. Xie, M. Liu, H.-C. Peng, N. Lu, J. Wang, M. J. Kim, and Y. Xia, "On the role of surface diffusion in determining the shape or morphology of noble-metal nanocrystals," Proc. Natl. Acad. Sci. U. S. A. **110**(17), 6669–6673 (2013).

[19] M. Meyns, F. Iacono, C. Palencia, J. Geweke, M. D. Coderch, U. E. A. Fittschen, J. M. Gallego, R. Otero, B. H. Juárez, and C. Klinke, "Shape evolution of CdSe nanoparticles controlled by halogen compounds," Chem. Mater. **26**(5), 1813–1821 (2014).

[20] S. Ghosh, R. Gaspari, G. Bertoni, M. C. Spadaro, M. Prato, S. Turner, A. Cavalli, L. Manna, and R. Brescia, "Pyramid-shaped wurtzite CdSe nanocrystals with inverted polarity," ACS Nano **9**(8), 8537–8546 (2015).

[21] G. Liu, H. G. Yang, J. Pan, Y. Q. Yang, G. Q. (Max) Lu, and H.-M. Cheng, "Titanium dioxide crystals with tailored facets," Chem. Rev. **114**(19), 9559–9612 (2014).

[22] S. Ghosh and L. Manna, "The many "facets" of halide ions in the chemistry of colloidal inorganic nanocrystals," Chem. Rev. **118**(16), 7804–7864 (2018).

[23] D. Seo, J. C. Park, and H. Song, "Polyhedral gold nanocrystals with O_h symmetry: From octahedra to cubes," J. Am. Chem. Soc. **128**(46), 14863–14870 (2006).

[24] S. Zhou, J. Li, K. D. Gilroy, J. Tao, C. Zhu, X. Yang, X. Sun, and Y. Xia, "Facile synthesis of silver nanocubes with sharp corners and edges in an aqueous solution," ACS Nano **10**(11), 9861–9870 (2016).

[25] L. J. Sherry, S.-H. Chang, G. C. Schatz, R. P. Van Duyne, B. J. Wiley, and Y. Xia, "Localized surface plasmon resonance spectroscopy of single silver nanocubes," Nano Lett. **5**(10), 2034–2038 (2005).

[26] T. B. Hoang, G. M. Akselrod, C. Argyropoulos, J. Huang, D. R. Smith, and M. H. Mikkelsen, "Ultrafast spontaneous emission source using plasmonic nanoantennas," Nat. Commun. **6**, 7788 (2015).

[27] C. Hrelescu, T. K. Sau, A. L. Rogach, F. Jäckel, and J. Feldmann, "Single gold nanostars enhance Raman scattering," Appl. Phys. Lett. **94**(15), 153113 (2009).

[28] P. L. Stiles, J. A. Dieringer, N. C. Shah, and R. P. V. Duyne, "Surface-enhanced Raman spectroscopy," Annu. Rev. Anal. Chem. **1**(1), 601–626 (2008).

[29] A. W. Jansons and J. E. Hutchison, "Continuous growth of metal oxide nanocrystals: Enhanced control of nanocrystal size and radial dopant distribution," ACS Nano **10**(7), 6942–6951 (2016).

[30] D. Ito, S. Yokoyama, T. Zaikova, K. Masuko, and J. E. Hutchison, "Synthesis of ligand-stabilized metal oxide nanocrystals and epitaxial core/shell nanocrystals via a lower-temperature esterification process," ACS Nano **8**(1), 64–75 (2014).

[31] M. V. Kovalenko, L. Manna, A. Cabot, Z. Hens, D. V. Talapin, C. R. Kagan, V. I. Klimov, A. L. Rogach, P. Reiss, D. J. Milliron *et al.*, "Prospects of nanoscience with nanocrystals," ACS Nano **9**(2), 1012–1057 (2015).

[32] C. B. Murray, D. J. Norris, and M. G. Bawendi, "Synthesis and characterization of nearly monodisperse CdE (E = sulfur, selenium, tellurium) semiconductor nanocrystallites," J. Am. Chem. Soc. **115**(19), 8706–8715 (1993).

[33] P. M. Allen, B. J. Walker, and M. G. Bawendi, "Mechanistic insights into the formation of InP quantum dots," Angew. Chem., Int. Ed. **49**(4), 760–762 (2010).

[34] M. C. Weidman, M. E. Beck, R. S. Hoffman, F. Prins, and W. A. Tisdale, "Monodisperse, air-stable PbS nanocrystals via precursor stoichiometry control," ACS Nano **8**(6), 6363–6371 (2014).

[35] G. Shen and P. Guyot-Sionnest, "HgS and HgS/CdS colloidal quantum dots with infrared intraband transitions and emergence of a surface plasmon," J. Phys. Chem. C **120**(21), 11744–11753 (2016).

[36] K. A. Willets and R. P. Van Duyne, "Localized surface plasmon resonance spectroscopy and sensing," Annu. Rev. Phys. Chem. **58**(1), 267–297 (2007).

[37] A. Dong, Y. Jiao, and D. J. Milliron, "Electronically coupled nanocrystal superlattice films by *in situ* ligand exchange at the liquid–air interface," ACS Nano **7**(12), 10978–10984 (2013).

[38] A. Dong, J. Chen, S. J. Oh, W. Koh, F. Xiu, X. Ye, D.-K. Ko, K. L. Wang, C. R. Kagan, and C. B. Murray, "Multiscale periodic assembly of striped nanocrystal superlattice films on a liquid surface," Nano Lett. **11**(2), 841–846 (2011).

[39] P. J. Winzer, D. T. Neilson, and A. R. Chraplyvy, "Fiber-optic transmission and networking: The previous 20 and the next 20 years [invited]," Opt. Express **26**(18), 24190–24239 (2018).

[40] G. Keiser, "Optical fiber communications," in *Wiley Encyclopedia of Telecommunications* (Wiley, 2003).

[41] G. M. Akselrod, C. Argyropoulos, T. B. Hoang, C. Ciracì, C. Fang, J. Huang, D. R. Smith, and M. H. Mikkelsen, "Probing the mechanisms of large purcell enhancement in plasmonic nanoantennas," Nat. Photonics **8**(11), 835–840 (2014).

[42] Y. Wu, G. Li, and J. P. Camden, "Probing nanoparticle plasmons with electron energy loss spectroscopy," Chem. Rev. **118**(6), 2994–3031 (2018).

[43] O. L. Krivanek, T. C. Lovejoy, N. Dellby, and R. W. Carpenter, "Monochromated STEM with a 30 MeV-wide, atom-sized electron probe," Microscopy **62**(1), 3–21 (2013).

[44] J. Spiegelberg, J. C. Idrobo, A. Herklotz, T. Z. Ward, W. Zhou, and J. Rusz, "Local low rank denoising for enhanced atomic resolution imaging," Ultramicroscopy **187**, 34–42 (2018).

[45] J. A. Hachtel, J. Huang, I. Popovs, S. Jansone-Popova, J. K. Keum, J. Jakowski, T. C. Lovejoy, N. Dellby, O. L. Krivanek, and J. C. Idrobo, "Identification of site-specific isotopic labels by vibrational spectroscopy in the electron microscope," Science **363**(6426), 525–528 (2019).

[46] B. H. Kim, C. M. Staller, S. H. Cho, S. Heo, C. E. Garrison, J. Kim, and D. J. Milliron, "High mobility in nanocrystal-based transparent conducting oxide thin films," ACS Nano **12**(4), 3200–3208 (2018).

[47] B. H. Toby and R. B. Von Dreele, "GSAS-II: The genesis of a modern open-source all purpose crystallography software package," J. Appl. Crystallogr. **46**(2), 544–549 (2013).

Published under license by AIP Publishing

[48] J. Li, L. Liu, and T.-K. Sham, "2D XANES–XEOL spectroscopy studies of morphology-dependent phase transformation and corresponding luminescence from hierarchical TiO_2 nanostructures," Chem. Mater. **27**(8), 3021–3029 (2015).

[49] R. G. Pearson, "Hard and soft acids and bases, HSAB, Part 1: Fundamental principles," J. Chem. Educ. **45**(9), 581 (1968).

[50] R. G. Pearson, "Hard and soft acids and bases, HSAB, part II: Underlying theories," J. Chem. Educ. **45**(10), 643 (1968).

[51] T. R. Gordon, M. Cargnello, T. Paik, F. Mangolini, R. T. Weber, P. Fornasiero, and C. B. Murray, "Nonaqueous synthesis of TiO_2 nanocrystals using TiF_4 to engineer morphology, oxygen vacancy concentration, and photocatalytic activity," J. Am. Chem. Soc. **134**(15), 6751–6761 (2012).

[52] H. G. Yang, C. H. Sun, S. Z. Qiao, J. Zou, G. Liu, S. C. Smith, H. M. Cheng, and G. Q. Lu, "Anatase TiO_2 single crystals with a large percentage of reactive facets," Nature **453**(7195), 638–641 (2008).

[53] A. Walsh and C. R. A. Catlow, "Structure, stability and work functions of the low index surfaces of pure indium oxide and Sn-doped indium oxide (ITO) from density functional theory," J. Mater. Chem. **20**(46), 10438–10444 (2010).

[54] J. Li, C. Liu, Y. Ye, J. Zhu, S. Wang, J. Guo, and T.-K. Sham, "Tracking the local effect of fluorine self-doping in anodic TiO_2 nanotubes," J. Phys. Chem. C **120**(8), 4623–4628 (2016).

[55] N. Karsi, P. Lang, M. Chehimi, M. Delamar, and G. Horowitz, "Modification of indium tin oxide films by alkanethiol and fatty acid self-assembled monolayers: A comparative study," Langmuir **22**(7), 3118–3124 (2006).

[56] H. Wang, K. Dou, W. Y. Teoh, Y. Zhan, T. F. Hung, F. Zhang, J. Xu, R. Zhang, and A. L. Rogach, "Engineering of facets, band structure, and gas-sensing properties of hierarchical Sn^{2+}-doped SnO_2 nanostructures," Adv. Funct. Mater. **23**(38), 4847–4853 (2013).

[57] H. Wang and A. L. Rogach, "Hierarchical SnO_2 nanostructures: Recent advances in design, synthesis, and applications," Chem. Mater. **26**(1), 123–133 (2014).

[58] G. Frank and H. Köstlin, "Electrical properties and defect model of tin-doped indium oxide layers," Appl. Phys. A **27**(4), 197–206 (1982).

[59] A. Comin and L. Manna, "New materials for tunable plasmonic colloidal nanocrystals," Chem. Soc. Rev. **43**(11), 3957–3975 (2014).

[60] K. Subba Ramaiah and V. Sundara Raja, "Structural and electrical properties of fluorine doped tin oxide films prepared by spray-pyrolysis technique," Appl. Surf. Sci. **253**(3), 1451–1458 (2006).

[61] Y. S. Avadhut, J. Weber, E. Hammarberg, C. Feldmann, I. Schellenberg, R. Pöttgen, and J. Schmedt auf der Günne, "Study on the defect structure of SnO_2:F nanoparticles by high-resolution solid-state NMR," Chem. Mater. **23**(6), 1526–1538 (2011).

[62] F. A. Kröger and H. J. Vink, "Relations between the concentrations of imperfections in crystalline solids," in *Solid State Physics*, edited by F. Seitz and D. Turnbull (Academic Press, 1956), Vol. 3, pp. 307–435.

[63] E. L. Runnerstrom, K. P. Kelley, E. Sachet, C. T. Shelton, and J.-P. Maria, "Epsilon-near-zero modes and surface plasmon resonance in fluorine-doped cadmium oxide thin films," ACS Photonics **4**(8), 1885–1892 (2017).

[64] J.-S. Seo, J.-H. Jeon, Y. H. Hwang, H. Park, M. Ryu, S.-H. K. Park, and B.-S. Bae, "Solution-processed flexible fluorine-doped indium zinc oxide thin-film transistors fabricated on plastic film at low temperature," Sci. Rep. **3**, 02085 (2013).

[65] T. Maruyama and T. Nakai, "Fluorine-doped indium oxide thin films prepared by chemical vapor deposition," J. Appl. Phys. **71**(6), 2915–2917 (1992).

[66] R. D. Shannon, "Revised effective ionic radii and systematic studies of interatomic distances in halides and chalcogenides," Acta Crystallogr., Sect. A **32**(5), 751–767 (1976).

[67] X.-D. Zhou and W. Huebner, "Size-induced lattice relaxation in CeO_2 nanoparticles," Appl. Phys. Lett. **79**(21), 3512–3514 (2001).

[68] N. Nadaud, N. Lequeux, M. Nanot, J. Jové, and T. Roisnel, "Structural studies of tin-doped indium oxide (ITO) and $In_4Sn_3O_{12}$," J. Solid State Chem. **135**(1), 140–148 (1998).

[69] F. E. Akkad and S. Joseph, "Physicochemical characterization of point defects in fluorine doped tin oxide films," J. Appl. Phys. **112**(2), 023501 (2012).

[70] S. D. Lounis, E. L. Runnerstrom, A. Llordes, and D. J. Milliron, "Defect chemistry and plasmon physics of colloidal metal oxide nanocrystals," J. Phys. Chem. Lett. **5**, 1564–1574 (2014).

[71] D. Mergel and Z. Qiao, "Dielectric modelling of optical spectra of thin In_2O_3 : Sn films," J. Phys. D: Appl. Phys. **35**(8), 794 (2002).

[72] I. Hamberg and C. G. Granqvist, "Evaporated Sn-doped In_2O_3 films: Basic optical properties and applications to energy-efficient windows," J. Appl. Phys. **60**(11), R123–R160 (1986).

[73] I. Hamberg and C. G. Granqvist, "Optical properties of transparent and heat-reflecting indium tin oxide films: The role of ionized impurity scattering," Appl. Phys. Lett. **44**(8), 721–723 (1984).

[74] E. Gerlach, "Carrier scattering and transport in semiconductors treated by the energy-loss method," J. Phys. C: Solid State Phys. **19**(24), 4585–4603 (1986).

[75] S. D. Lounis, E. L. Runnerstrom, A. Bergerud, D. Nordlund, and D. J. Milliron, "Influence of dopant distribution on the plasmonic properties of indium tin oxide nanocrystals," J. Am. Chem. Soc. **136**(19), 7110–7116 (2014).

[76] E. L. Runnerstrom, A. Bergerud, A. Agrawal, R. W. Johns, C. J. Dahlman, A. Singh, S. M. Selbach, and D. J. Milliron, "Defect engineering in plasmonic metal oxide nanocrystals," Nano Lett. **16**(5), 3390–3398 (2016).

[77] R. Bel Hadj Tahar, T. Ban, Y. Ohya, and Y. Takahashi, "Tin doped indium oxide thin films: Electrical properties," J. Appl. Phys. **83**(5), 2631–2645 (1998).

[78] B. Tandon, S. Ghosh, and D. J. Milliron, "Dopant selection strategy for high-quality factor localized surface plasmon resonance from doped metal oxide nanocrystals," Chem. Mater. **31**, 7752 (2019).

[79] K. Miszta, J. de Graaf, G. Bertoni, D. Dorfs, R. Brescia, S. Marras, L. Ceseracciu, R. Cingolani, R. van Roij, M. Dijkstra *et al.*, "Hierarchical self-assembly of suspended branched colloidal nanocrystals into superlattice structures," Nat. Mater. **10**(11), 872–876 (2011).

[80] J. M. Pietryga, Y.-S. Park, J. Lim, A. F. Fidler, W. K. Bae, S. Brovelli, and V. I. Klimov, "Spectroscopic and device aspects of nanocrystal quantum dots," Chem. Rev. **116**(18), 10513–10622 (2016).

[81] B. A. Korgel, S. Fullam, S. Connolly, and D. Fitzmaurice, "Assembly and self-organization of silver nanocrystal superlattices: Ordered "soft spheres"," J. Phys. Chem. B **102**(43), 8379–8388 (1998).

[82] J. T. Hugall, A. Singh, and N. F. van Hulst, "Plasmonic cavity coupling," ACS Photonics **5**(1), 43–53 (2018).

[83] M. Pelton, "Modified spontaneous emission in nanophotonic structures," Nat. Photonics **9**(7), 427–435 (2015).

[84] A. Singh, P. M. de Roque, G. Calbris, J. T. Hugall, and N. F. van Hulst, "Nanoscale mapping and control of antenna-coupling strength for bright single photon sources," Nano Lett. **18**(4), 2538–2544 (2018).

[85] A. F. Kockum, A. Miranowicz, S. D. Liberato, S. Savasta, and F. Nori, "Ultrastrong coupling between light and matter," Nat. Rev. Phys. **1**(1), 19 (2019).

[86] P. Vasa and C. Lienau, "Strong light–matter interaction in quantum emitter/metal hybrid nanostructures," ACS Photonics **5**(1), 2–23 (2018).

[87] P. Vasa, W. Wang, R. Pomraenke, M. Lammers, M. Maiuri, C. Manzoni, G. Cerullo, and C. Lienau, "Real-time observation of ultrafast Rabi oscillations between excitons and plasmons in metal nanostructures with J-aggregates," Nat. Photonics **7**(2), 128–132 (2013).

[88] E. M. Purcell, "Spontaneous emission probabilities at radio frequencies," in *Confined Electrons and Photons: New Physics and Applications*, NATO ASI Series, edited by E. Burstein and C. Weisbuch (Springer US, Boston, MA, 1995), p. 839.

[89] M. Fox, *Quantum Optics: An Introduction* (Oxford University Press USA-OSO, Oxford, United Kingdom, 2006).

[90] R. Coccioli, M. Boroditsky, K. W. Kim, Y. Rahmat-Samii, and E. Yablonovitch, "Smallest possible electromagnetic mode volume in a dielectric cavity," IEE Proc.: Optoelectron. **145**(6), 391–397 (1998).

[91] C. Sauvan, J. P. Hugonin, I. S. Maksymov, and P. Lalanne, "Theory of the spontaneous optical emission of nanosize photonic and plasmon resonators," Phys. Rev. Lett. **110**(23), 237401 (2013).

Published under license by AIP Publishing

[92] J.-M. Gérard, "Solid-state cavity-quantum electrodynamics with self-assembled quantum dots," in *Single Quantum Dots: Fundamentals, Applications, and New Concepts; Topics in Applied Physics* (Springer Berlin Heidelberg, Berlin, Heidelberg, 2003), pp. 269–314.

[93] R. Chikkaraddy, B. de Nijs, F. Benz, S. J. Barrow, O. A. Scherman, E. Rosta, A. Demetriadou, P. Fox, O. Hess, and J. J. Baumberg, "Single-molecule strong coupling at room temperature in plasmonic nanocavities," Nature **535**(7610), 127–130 (2016).

[94] P. T. Kristensen and S. Hughes, "Modes and mode volumes of leaky optical cavities and plasmonic nanoresonators," ACS Photonics **1**(1), 2–10 (2014).

[95] F.-P. Schmidt, H. Ditlbacher, U. Hohenester, A. Hohenau, F. Hofer, and J. R. Krenn, "Dark plasmonic breathing modes in silver nanodisks," Nano Lett. **12**(11), 5780–5783 (2012).

[96] W. Fang, J. Y. Xu, A. Yamilov, H. Cao, Y. Ma, S. T. Ho, and G. S. Solomon, "Large enhancement of spontaneous emission rates of InAs quantum dots in GaAs microdisks," Opt. Lett. **27**(11), 948–950 (2002).

[97] J. Yuen-Zhou, S. K. Saikin, T. Zhu, M. C. Onbasli, C. A. Ross, V. Bulovic, and M. A. Baldo, "Plexciton Dirac points and topological modes," Nat. Commun. **7**, 11783 (2016).

[98] M. Parzefall and L. Novotny, "Light at the end of the tunnel," ACS Photonics **5**(11), 4195–4202 (2018).

[99] D. Wang, J. Guan, J. Hu, M. R. Bourgeois, and T. W. Odom, "Manipulating light–matter interactions in plasmonic nanoparticle lattices," Acc. Chem. Res. **52**, 2997 (2019).

[100] S. A. Maier, "Plasmonic field enhancement and SERS in the effective mode volume picture," Opt. Express **14**(5), 1957–1964 (2006).

[101] U. Aslam, V. G. Rao, S. Chavez, and S. Linic, "Catalytic conversion of solar to chemical energy on plasmonic metal nanostructures," Nat. Catal. **1**(9), 656 (2018).

[102] C. Zhan, X.-J. Chen, J. Yi, J.-F. Li, D.-Y. Wu, and Z.-Q. Tian, "From plasmon-enhanced molecular spectroscopy to plasmon-mediated chemical reactions," Nat. Rev. Chem. **2**(9), 216 (2018).

[103] J. D. Caldwell, I. Aharonovich, G. Cassabois, J. H. Edgar, B. Gil, and D. N. Basov, "Photonics with hexagonal boron nitride," Nat. Rev. Mater. **4**(8), 552–567 (2019).

[104] K. Miyata, D. Meggiolaro, M. T. Trinh, P. P. Joshi, E. Mosconi, S. C. Jones, F. D. Angelis, and X.-Y. Zhu, "Large polarons in lead halide perovskites," Sci. Adv. **3**(8), e1701217 (2017).

[105] D. Sanvitto and S. Kéna-Cohen, "The road towards polaritonic devices," Nat. Mater. **15**(10), 1061–1073 (2016).

[106] R. F. Ribeiro, L. A. Martínez-Martínez, M. Du, J. Campos-Gonzalez-Angulo, and J. Yuen-Zhou, "Polariton chemistry: Controlling molecular dynamics with optical cavities," Chem. Sci. **9**(30), 6325–6339 (2018).

Published under license by AIP Publishing